











Please cite the Published Version

Peeters, J , Graham, A , Toonen, WHJ , Pennington, BT , Durcan, JA , Winkels, TG , Barker, DS, Masson-Berghoff, A , Adamson, K , Emery, VL, Strutt, KD, Millet, M , Sollars, LH and Ghazala, HH  (2024) Shift away from Nile incision at Luxor 4,000 years ago impacted ancient Egyptian landscapes. *Nature Geoscience*. ISSN 1752-0894

DOI: <https://doi.org/10.1038/s41561-024-01451-z>

Publisher: Springer

Version: Published Version

Downloaded from: <https://e-space.mmu.ac.uk/634843/>

Usage rights:  [Creative Commons: Attribution 4.0](https://creativecommons.org/licenses/by/4.0/)

Additional Information: This is an open access article published in *Nature Geoscience*, by Springer.

Data Access Statement: The datasets generated and analysed for this study are available in the main text, Methods, Extended Data and/or Supplementary Data 1. In addition, our sediment core dataset is also openly available via Zenodo at <https://doi.org/10.5281/zenodo.10813774> (ref. 66).

Enquiries:

If you have questions about this document, contact openresearch@mmu.ac.uk. Please include the URL of the record in e-space. If you believe that your, or a third party's rights have been compromised through this document please see our Take Down policy (available from <https://www.mmu.ac.uk/library/using-the-library/policies-and-guidelines>)

Shift away from Nile incision at Luxor ~4,000 years ago impacted ancient Egyptian landscapes

Received: 8 March 2023

Accepted: 12 April 2024

Published online: 29 May 2024

 Check for updates

Jan Peeters^{1,2}, Angus Graham³✉, Willem H. J. Toonen^{4,5}, Benjamin T. Pennington^{6,7}, Julie A. Durcan⁸, Timotheus G. Winkels⁹, Dominic S. Barker¹⁰, Aurélia Masson-Berghoff¹¹, Kathryn Adamson¹², Virginia L. Emery¹³, Kristian D. Strutt¹⁰, Marie Millet¹⁴, Luke H. Sollars¹⁵ & Hosni H. Ghazala¹⁶

Although the Nile is one of the largest rivers in the world and played a central role in ancient Egyptian life, little is known about its response to climatic change during the Holocene. Here we present a framework for the evolution of the Egyptian Nile, demonstrating how climatic and environmental changes have shaped the landscape of the Egyptian Nile Valley over the past 11,500 years, including the civilization of ancient Egypt (~5,000 to 2,000 years ago). Using data from over 80 sediment cores drilled in a transect spanning the Nile Valley near Luxor, pinned in time by 48 optically stimulated luminescence ages, we reconstruct the dynamics of the Nile River during the Holocene in the vicinity of UNESCO World Heritage sites such as Karnak and Luxor temples. According to our reconstruction, valley incision occurred from the start of the record until approximately 4,000 years ago and then rapidly shifted to massive floodplain aggradation. We argue that this relatively abrupt change in the riverine landscape near Luxor from the Middle to Late Holocene was linked to a shift towards a drier regional hydroclimate around this time. Such a dramatic change in river sediment dynamics could have had local agro-economic consequences.

The River Nile forms the fertile corridor that links its headwaters in equatorial Africa to its delta in the Mediterranean (Fig. 1)¹. An understanding of its evolution through the Holocene is pivotal to discussions of fluvial system dynamics and ancient cultural development, which both occurred against a backdrop of major hydroclimatic change: that is, the shift from the ‘Green Sahara’ of the African Humid Period (-14.5–5.0 thousand years ago (ka))^{2–5} to the present hyper-arid Sahara Desert^{6,7}. The present understanding of the Egyptian Nile’s response to climate change relies heavily on data gathered from its delta^{8,9}, its offshore Mediterranean deep-sea fan^{4,10–13} and the Fayum depression¹⁴. Few studies have focused on the fluvial domain itself^{15–17}, and very little is known about the Holocene development of the Egyptian

Nile Valley^{18–21} despite its central role in ancient Egyptian history^{22,23}. Furthermore, previous research on the Egyptian Nile is often lacking detailed chronostratigraphic and sedimentological data that make existing reconstructions highly uncertain and inconsistent^{22,24}.

To address this knowledge gap, a transect of 81 boreholes spanning the Nile Valley (-10 km wide) was drilled near Luxor (ancient Thebes) in Upper Egypt (Fig. 1). Sedimentary information from these cores (average depth -8 m) (Supplementary Data 1) was used to study key changes in the riverine landscape, which are pinned in time by 48 optically stimulated luminescence (OSL) ages (Extended Data Figs. 1–4 and Extended Data Tables 1–4). This approach provides a unique and vital understanding of the Holocene Egyptian Nile system

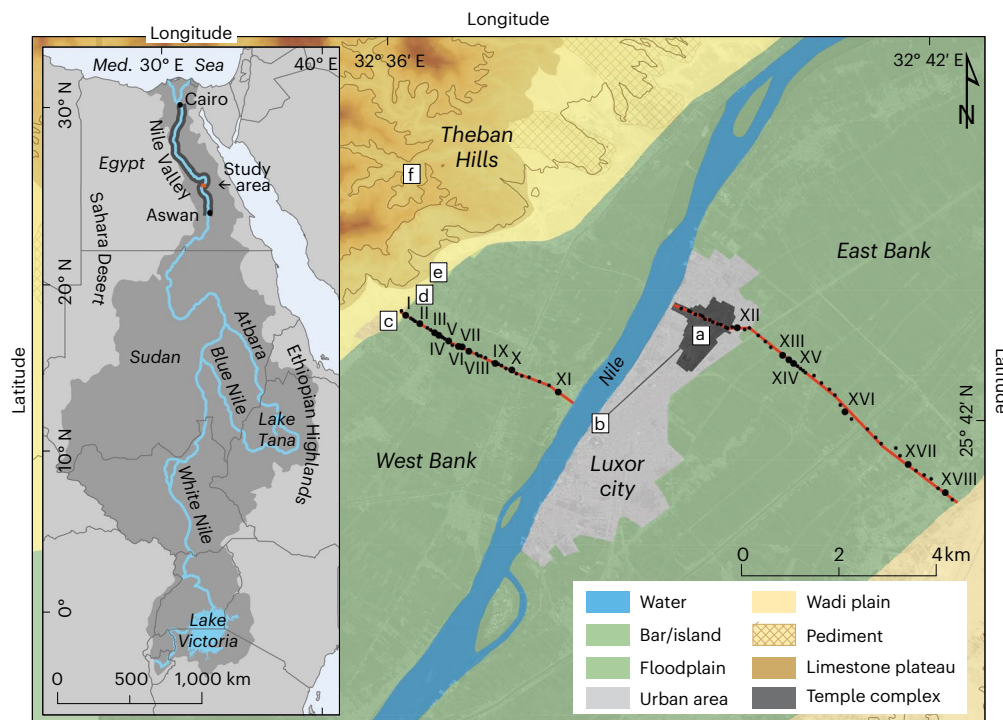


Fig. 1 | Geomorphic map of the Nile Valley near Luxor, Egypt. Smaller black dots mark borehole locations; larger black dots mark OSL-dated core sites and are labelled with Roman numerals. **a–f**, Key archaeological sites: Karnak Temple complex (**a**), Luxor Temple (**b**), Medinet Habu (**c**), Kom el-Hettân (**d**), Ramesseum (**e**) and Valley of the Kings (**f**). The inset map shows the Nile Basin

(dark grey) in Northeast Africa, its drainage system (blue) and the Egyptian Nile Valley (black). Methods provide more OSL dating details, and Extended Data Tables 1 and 3 provide cross references with original core-site numbering. Med., Mediterranean. Figure created using ArcGIS Pro. Credit: background World Imagery Basemap, Esri.

and its responses to climate change at a focal region of ancient Egyptian culture. Our area of investigation includes UNESCO World Heritage sites such as the Karnak and Luxor temples located east of the present Nile (Fig. 1) and the royal cult temples and necropoleis on the western desert margin—places that were both physically and mythologically connected to the fluvial landscape^{25,26}. In addition, it is possible that the changing environment also impacted the regional agro-economy, which was of critical importance to the success of the ancient Egyptian state^{27,28}.

Our study shows how the floodplain environment changed dramatically during the Dynastic Period (–5.1–2.4 ka) (Extended Data Table 5) and how the environmental canvas on which ancient culture developed, thrived and declined was reshaped. We introduce a framework for the Egyptian Nile near Luxor, while also filling in the looming gap in hydroclimatic information that exists between upstream and downstream locations within the Nile Basin²⁹.

Sedimentary architecture of Holocene Egyptian Nile Valley

At various levels in the subsurface along our transect near Luxor, the borehole data reveal basal, sandy deposits, which are interpreted as fluvial terraces (units T1–4; Fig. 2 and Table 1). These erosional terraces are the result of long-term semi-continuous valley-wide fluvial incision and contraction during the first half of the Holocene. Subsequently, a shift occurred to a fast-aggrading Nile system during the remainder of the Holocene, whose deposits blanketed the earlier terrace morphology. Multiple channel belts (units CB1–3b) and a laterally expanding floodplain (unit FP1) are associated with this more recent phase of fluvial aggradation and valley expansion.

The oldest terrace (T1; Fig. 2 and Table 1) is dated to 9.42 ± 0.75 ka and forms the oldest present-day exposed surface at the eastern valley margin at an elevation of –78.5 m above mean sea level. Westward, buried underneath –1 m of younger alluvium, the top of terrace T2 lies

at –75 m and is dated to 8.85 ± 0.66 ka. Further towards the centre of the valley, the top of terrace T3, at 70–72 m, is dated to 4.54 ± 0.42 ka; a small remnant of T3 is also preserved at the West Bank's desert edge. The youngest terrace, T4, at 66–68 m, is dated to 4.09 ± 0.31 ka and is only found on the West Bank. This terrace forms the substrate from which fluvial aggradation initiated and thus marks an important turning point in the fluvial history of the Nile Valley.

Three channel belts (CB1–3) can be distinguished in the transect (Fig. 2 and Table 1), with (the end of) their activity dated to 3.34 ± 0.27 ka (CB1), 2.81 ± 0.21 ka (CB2) and 0.11 ± 0.01 ka (CB3) respectively. CB3b comprises the present-day Nile. CB1 is 500–600 m wide and corresponds in age and geometry with a previously studied secondary river channel on the Theban West Bank^{26,30}. CB2 measures –1,200 m across and so may have carried the Nile's full discharge. CB3 is –1,800 m wide and was partially abandoned during the first half of the twentieth century³¹. The modern Nile belt (CB3b) is 600–750 m wide. Its channel is presently entrenched by 2–3 m, probably in response to sediment deprivation due to the construction of the Aswan High Dam in the 1960s.

Floodplain deposits (FP1; Table 1) blanket both banks, varying in thickness between 1 and 1.5 m in the east to –9.5 m in the west (Fig. 2). Eight OSL ages at core-site VII determined floodplain sedimentation rates at –12 mm per year around 3.4 ka (that is, New Kingdom age; Extended Data Table 5), whereas rates of the last three millennia were substantially lower at –2 mm per year (Extended Data Fig. 5).

Hydroclimatic impact on the Nile's evolution

Our research reveals a major shift in the Nile's fluvial system behaviour, a turning point largely unrecognized in its phasing, time frame and mechanism in previous Nile river dynamics models^{22,23,29} and adds to other studies that have inferred Holocene deposition^{19,24,28}. We found a sequence of channel entrenchment and contraction during the Early and Middle Holocene (Fig. 3a–d) that completely reverts to valley-wide

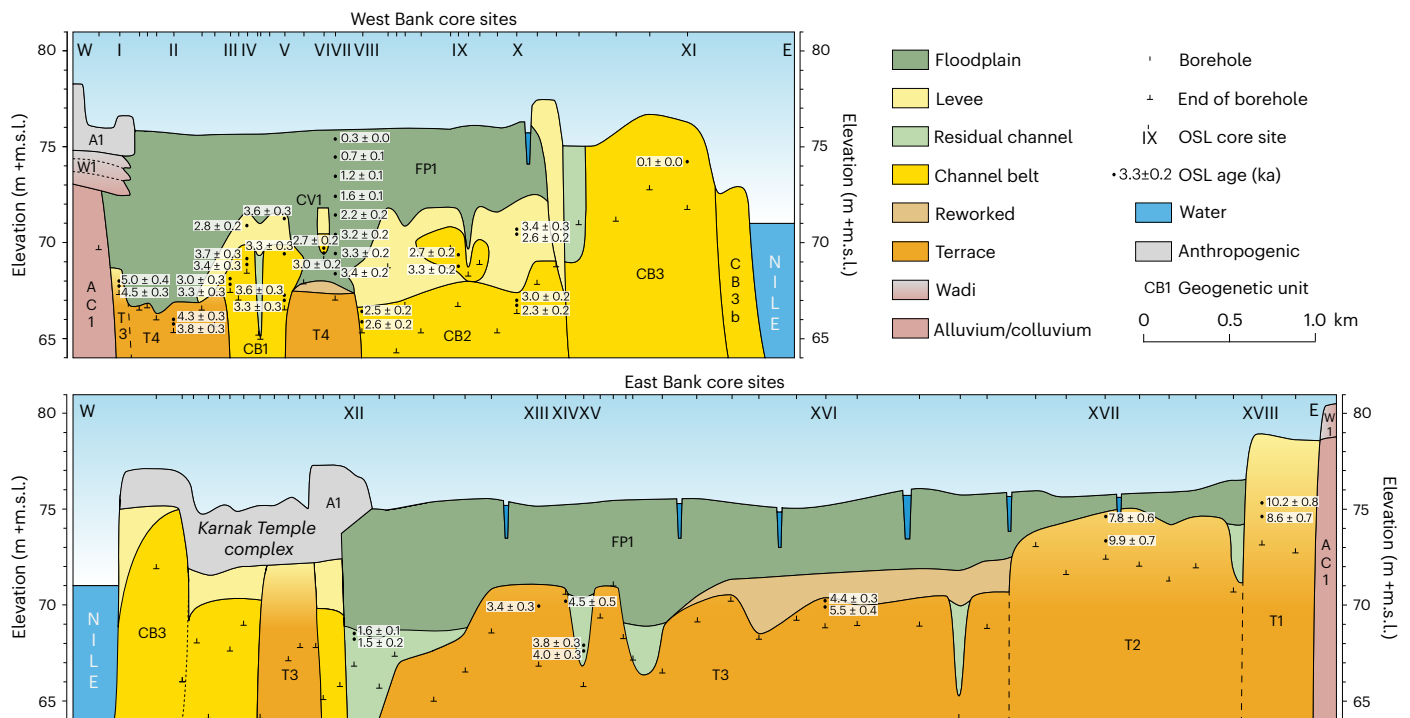


Fig. 2 | Sedimentary architecture of the Holocene Nile Valley near Luxor, Egypt. Figure 1 provides transect and OSL-dated core-site locations. OSL ages are shown with only one decimal for legibility; Methods and Extended Data Figs. 1–4

and Tables 1–4 provide a comprehensive account of the OSL dating. Table 1 provides sedimentary descriptions and facies interpretation of each geogenetic unit. W, west; E, east; +m.s.l., above mean sea level.

fluvial aggradation around 4 ka (Figs. 3e–h and 4a), potentially coinciding with the 4.2 ka climate event³². Such system changes are usually related to a (combination of) substantial increase in sediment supply, sediment fining and/or a decrease in discharge³³, forced by changes in the hydroclimatic regime.

The changes observed here in the Egyptian Nile’s Holocene riverine landscape near Luxor are in line with observations of their drivers (Fig. 4b–g), evidence for which is found elsewhere in the Nile Basin. From -11.5 ka onward, wet conditions existed over northern Africa (Fig. 4d,e,^{6,7,34–36}), due to a northern position of the Intertropical Convergence Zone⁴, which resulted in increased Nile discharge enlarging its erosivity and transport capacity (Fig. 4f)^{11–13,37}. Wetter conditions also led to a denser vegetative cover^{6,7}, reducing upstream sediment input (Fig. 4g)^{11,12,38}. The observed erosion and subsequent uptake of sediment in the Nile Valley through channel incision was, therefore, probably a direct result of the wetter Early Holocene Nile Basin’s hydroclimatic regime.

Conversely, rapid aggradation and formation of CB1–3b in the Nile Valley from -4 ka onward is thought to have been triggered by a diminishing discharge (and hence erosion capacity) and an increase in (fine) sediment supply^{11,12,17,39}. The driving factor behind this increase was the progressive aridification of the Nile Basin, especially between 5 and 6 ka (Fig. 4c,¹)^{3,6,34,40}, which, potentially in combination with changing human impact on the hinterland^{41–43}, made soils increasingly prone to erosion⁴⁴.

This major shift in the Nile’s system led to progressive changes in the fluvial planform of the Egyptian Nile near Luxor (Fig. 4h), from a dynamic wandering-braided system (T1–4) during its incisive phase (-11.5–4 ka), to less-dynamic anabranching straight channels (CB1–2 and CB3’s predecessor) during its transition (-4–2 ka) (Fig. 3e,f) and the present single-thread system (CB3(b)) during its most recent phase (-2 ka–present) (Fig. 3g,h). The large input of fine sediment promoted cohesive bank and floodplain formation, enhancing their erosion-resistance and progressively securing the low-gradient

channels (CB1–3) in their position. Limited migration facilitated the build-up of natural levees and increased the elevation difference with the backswamp areas. This led to rearrangement of the Egyptian Nile’s channel configuration in an avulsive manner following levee breaches during high flood stages^{21,26}, rather than gradual lateral migration as has been previously suggested for the presumed meandering Egyptian Nile system^{22,23}.

On a supraregional scale, these changing hydroclimatic conditions led to increased fluvial dynamics, and in combination with sea-level rise in the Mediterranean^{8,9}, resulted in the onlap of alluvium and creation of floodplains in downstream regions from 7–8 ka ago. Over time, the Nile’s depocentres shifted progressively upstream, from the Nile’s deep-sea fan all the way up to Upper Egypt, implying diachronous onsets in aggradation (Fig. 4i–k) and basically backfilling its valley. The increase in sediment supply, in combination with a reduction in discharge, and helped by a deceleration of Late Holocene sea-level rise, will have accelerated the upstream movement of the location where the river started to aggrade.

Before -8 ka, most of the sedimentation occurred on the western deep-sea fan, with records showing accumulation rates of >1 mm per year (Fig. 4i)^{10,11}. From -8–5.5 ka, sedimentation on the deep-sea fan notably slowed down, whereas the Nile Delta started to build up at rates of >2 mm per year (Fig. 4j)⁹. Here the erosion upstream in the Nile Valley, together with rising Holocene sea levels, led to enhanced aggradation^{9,45}. From -5.5–4 ka, sedimentation on the Nile’s deep-sea fan remained low, whereas deposition in the delta dwindled to 0.5–1.5 mm per year (Fig. 4i,j)⁹. Instead, sedimentation increased in the downstream end of the Nile Valley, where aggradation started around 7.7 ka ago²⁰. In Middle Egypt, aggradation started before -4.5 ka (ref. 21), earlier than the onset of aggradation near Luxor. From 4 to 3 ka, rapid floodplain aggradation in the still-confined valley setting peaked with sedimentation rates of -12 mm per year in the Nile Valley near Luxor (Fig. 4k), while remaining low in the delta. After -3 ka and until the present, sedimentation in the Nile Valley progressively slowed

Table 1 | Overview of geogenetic units in the Holocene Nile Valley near Luxor, Egypt

Geogenetic unit	West/East Bank	Dominant texture(s), sedimentary structures	Facies interpretation	Age (ka) ^a
A1	WB+EB	Highly variable heterogeneous loamy textures—that is, clay loam to sandy loam, very poorly sorted, often containing large quantities of admixed ceramic sherds, stone (chips), bone fragments and so on.	Anthropogenic foundation, construction and/or area of activity.	Circa 3.25/2–4
FP1	WB+EB	Homogeneous fine-grained, very well-sorted silty clay to silty clay loam (5–30 μm), often containing calcareous rhizoliths at distinct levels. On the WB, individually aeolian-transported sand grains (~250 μm) are found dispersed within the matrix, with a higher abundance towards its top.	Floodplain; Nilotic overbank deposits containing paleosols.	>3.42±0.23–completion Aswan High Dam
CB3b	WB	Well-sorted sand (150–350 μm), cross bedded and often containing gravel. Pebbles (2–5 cm) are found in the thalweg.	Channel belt; riverbed incised 2–3 m since 1970.	Present-day Nile River
CB3	WB+EB	Cross-bedded, well-sorted sand (150–300 μm), often with high mica content, cm-scale laminations and some gravel; fining upward into coarse silt and fine loam (20–60 μm) with frequent sub-centimetre laminations. Two stacked fining-upward sequences consisting of laminated well-sorted, mica-rich sandy loams and loamy sands (80–250 μm) are found in a topographic depression.	Channel belt; including its levee and residual channel.	0.11±0.01
CB2	WB	Well-sorted, mica-rich very fine to medium sand (75–300 μm), cross bedded and occasionally laminated. Laterally more variable than the other CB units. Fining upward into somewhat heterogeneous textures: silt loam, silt, sandy loam and very fine sand (30–75 μm); all laminated. The central upper part of this unit consists of very fine to fine-grained (loamy) sand (75–200 μm).	Channel belt; including its levee, residual channel, probably distinctive bars/islands and possibly a reactivation phase.	2.81±0.21
CB1	WB	Well-sorted, mica-rich fine- to medium-grained sand (100–250 μm), cross bedded, often with cm lamination; fining upward into (sandy) loam (60–75 μm), often containing large quantities of ceramic sherds. Black-coloured, mm-laminated (silt) loam (40–60 μm) is found in the centre of this unit at relatively great depth.	Channel belt; including its levee and residual channel.	3.34±0.27
CV1	WB	Isolated, relatively short sequence of well-sorted, loamy sand (100 μm) fining upward into very well-sorted silt (40 μm), both being rich in mica.	Crevasse; introduced during Nilotic flood(s).	2.83±0.21
T4	WB	Moderately to well-sorted, mica-rich fine-grained sand (150–250 μm). ^b	Fluvial terrace; possibly with a partially reworked top.	4.09±0.31
T3	WB+EB	Repetitive, short (~1 m thick) stacked fining-upward sequences with poorly to moderately sorted, fine to coarse-grained to coarse-grained sand (150–700 μm) often with gravel towards the base of the sets. Multiple sequences of more heterogeneous, laminated, finer-grained textures: that is, clay, silt and sandy loam (40–100 μm); containing large quantities of ceramic sherds in the west. Eastern half of the EB unit is covered by finer-grained, laterally heterogeneous textures: silt and sandy loam (60–100 μm) with occasionally dm-thick sand lenses (125–300 μm).	Fluvial terrace; including multiple residual channels and possibly a partially reworked cover.	4.54±0.42
T2	EB	Repetitively stacked fining-upward sequences (2–4 m thick) with poorly to moderately sorted, medium- to coarse-grained sand (250–800 μm) with gravel towards the base of the sets; well-sorted mica containing sandy loam and loamy sand (75–250 μm) are found towards the top of the sequences. A more heterogeneous, finer-grained (40–75 μm) sequence is found at the eastern limit of this unit, consisting of mica-rich sand and silt loam.	Fluvial terrace; including a residual channel.	8.85±0.66
T1	EB	Repetitive, relatively short (2–3 m), stacked fining-upward sequences with poorly to moderately sorted, fine- to coarse-grained sand (150–650 μm), often containing cm laminations and gravel towards the base of the sets; mica-rich loamy sand and fine sand (80–150 μm) towards its top.	Fluvial terrace.	9.42±0.75
W1	WB	Loosely consolidated, very poorly sorted (sub-)rounded gravel (1–5 cm) of polygenetic origin in a matrix of very poorly sorted, fine to very coarse to very coarse sand (200–1,500 μm).	(Sub-)recent wadi alluvium.	Holocene
AC1	WB+EB	Massive, somewhat consolidated rounded to subrounded gravel of polygenetic origin in a matrix of coarse sand/cross-bedded fluvial sand with minor conglomerate and clay beds.	Colluvium/alluvium; deposited by locally fed ephemeral streams.	Pleistocene (Pre Nile)

Note: Sedimentary texture description conforms to United States Department of Agriculture standards⁴⁷. ^aAges are based on luminescence dates, historical maps and literature sources. Methods provide luminescence dating details. ^bDue to its deeply-buried position—that is, 8–10 m beneath the surface, core penetration of T4 was often limited to <1 m.

to ~2 mm per year. Further upstream beyond Aswan, no such alluvial onlap is found as base levels were controlled by the Nile cataracts. This also hampers a direct comparison of fluvial dynamics of the Egyptian Nile and the Sudanese Desert Nile¹⁶.

The decline in floodplain sedimentation in the Nile Valley near Luxor is accompanied by regional Calcisol formation (Table 1), signalling a temporary stagnation of Nilotic overbank deposition during ~3.1–2.7 ka that was previously associated with a period of lower flow during the late New Kingdom to Third Intermediate Period (Extended

Data Table 5)^{26,29,30}. Yet, our insights indicate that this cannot be fully attributed to reduced flow conditions of the Nile, as the reduced accumulation rates also reflect substantial lateral expansion of the Nile's floodplain, which doubled in width around 2.8 ka (Fig. 3f) as pre-existing high terrace levels were re-submerged by ongoing aggradation.

Impacts on the ancient Egyptian landscape

Variations in ancient and recent Nile floods are often discussed in terms of their impacts on Egyptian society^{22,29,46}. The Early and Middle

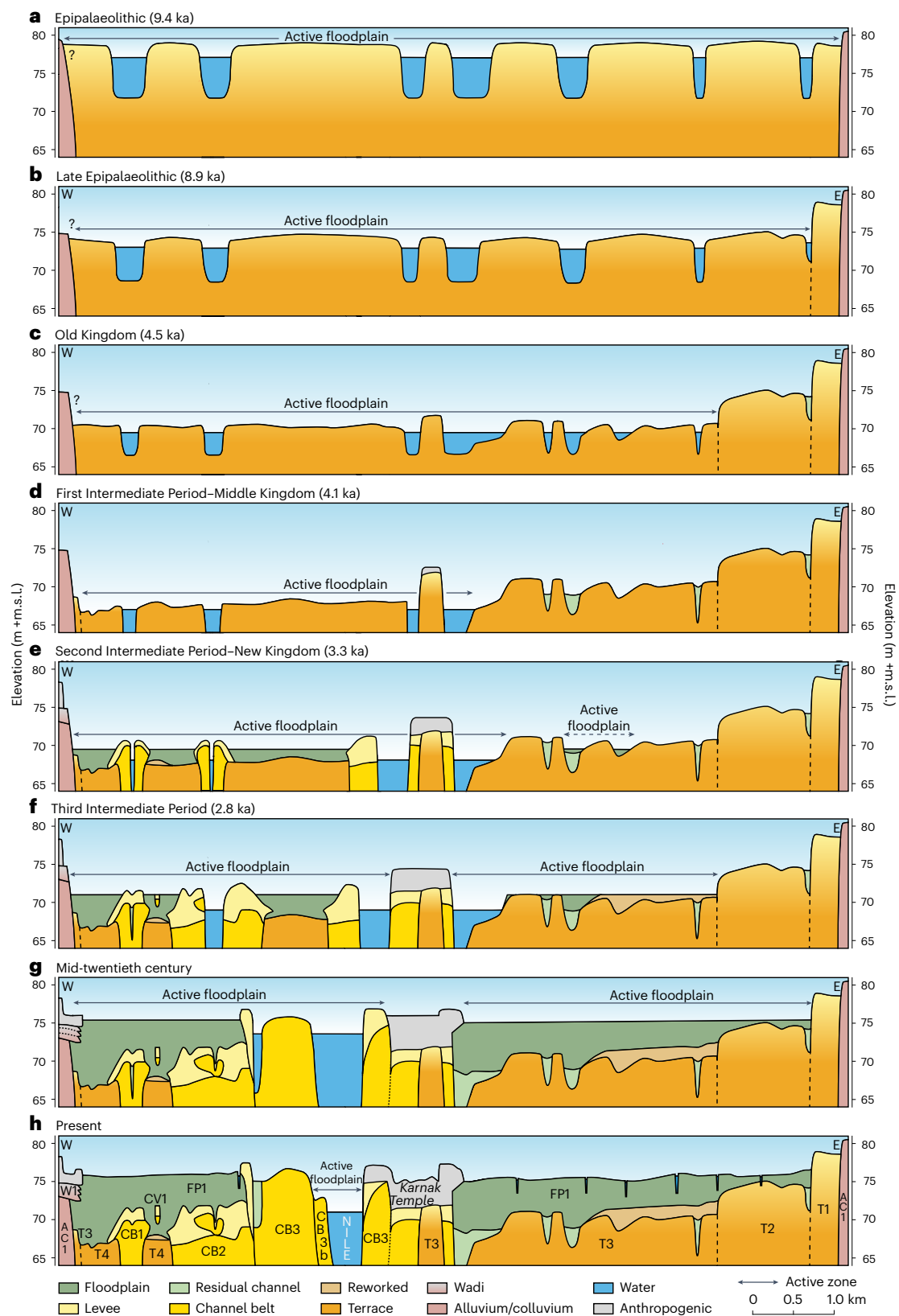


Fig. 3 | Schematic reconstruction of the Holocene evolution of the Nile River near Luxor, Egypt. **a–d**, During the Early and Middle Holocene (**a**), Epipalaeolithic deposits were incised by ~3.5 m during the Late Epipalaeolithic (**b**), which were subsequently incised by 3–5 m during the Old Kingdom (**c**) and again during the Middle Kingdom (**d**) by another 2–4 m, forming the Nile Valley’s substrate, while consistently narrowing its active floodplain at each erosional

step. **e–g**, From the New Kingdom (**e**) onward, fluvial aggradation and channel belt formation starts and continued during the Third Intermediate Period (**f**) until the mid-twentieth century (**g**) when upstream dam construction started to reduce sediment supply. **h**, Until recently, the Nile River managed to gradually build up and enlarge its floodplain, eventually spanning almost its entire valley. Egyptian cultural periods: Extended Data Table 5; ages (ka): Table 1.

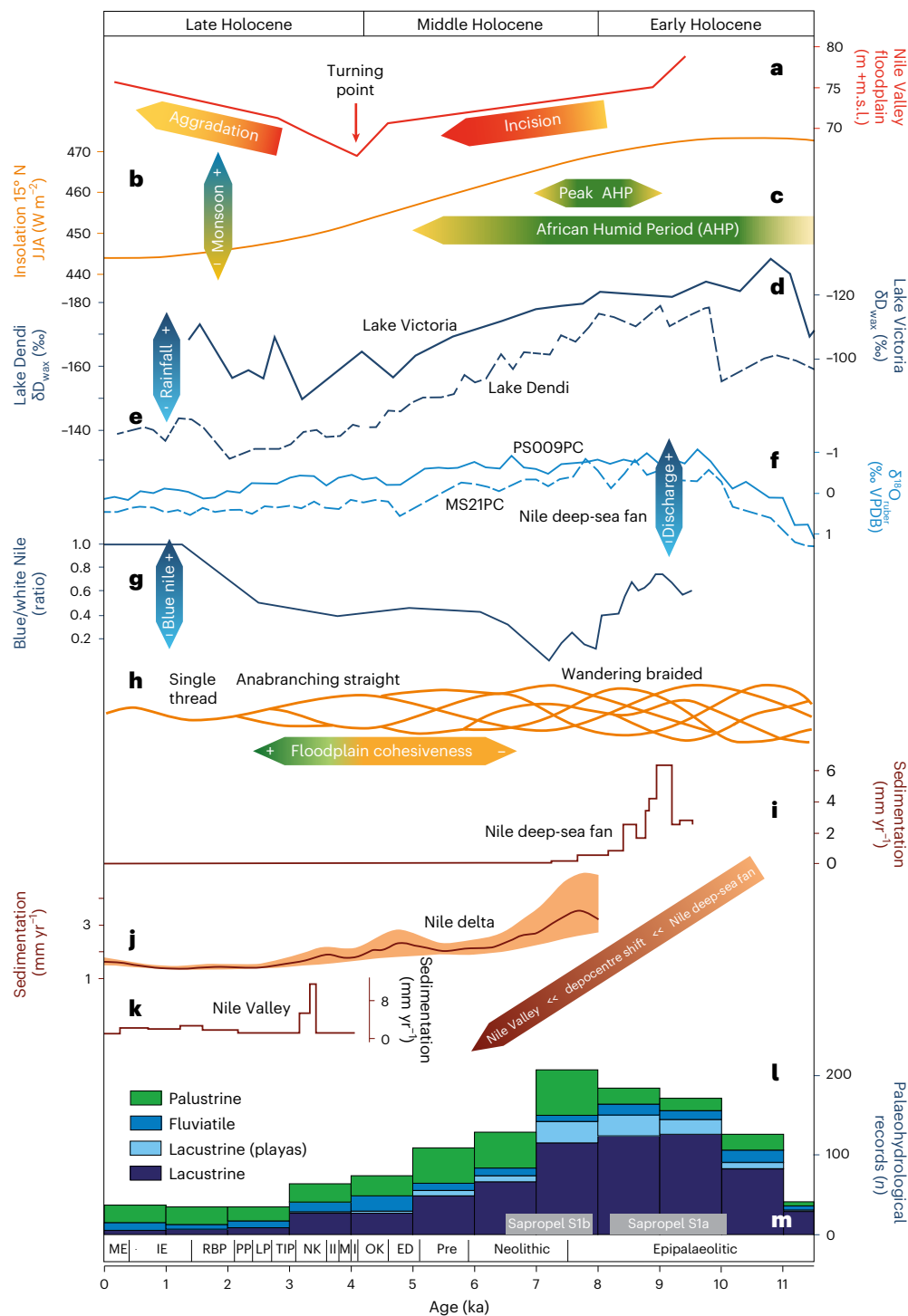


Fig. 4 | Synthesis of the Egyptian Nile Valley's fluvial evolution in relation to hydroclimatic changes in the Nile Basin. a, Nile Valley floodplain incision and aggradation levels (this study). **b**, Summer insolation (June, July, August (JJA)) at 15° N (ref. 48) as indicator for monsoon strength. **c**, Duration of the African Humid Period (AHP)³; peak AHP⁴. **d, e**, Hydrogen isotope record from leaf waxes (δD_{wax}) as proxy for precipitation variation in the Lake Victoria basin (**d**)³⁵ and the Ethiopian Highlands (Lake Dendi)³⁶ (**e**). **f**, *Globigerinoides ruber* oxygen isotope as a proxy for Nile discharge recorded on its deep-sea fan. MS21PC: central

deep-sea fan; PS009PC: eastern deep-sea fan¹². **g**, Blue/white Nile provenance in deep-sea fan sediments¹¹. **h**, Fluvial planform of the Nile River near Luxor (this study). **i–k**, Sedimentation rates (mm yr^{-1}) for the Nile deep-sea fan¹¹ (**i**), spatially averaged values for the northern Nile Delta⁴⁵ (**j**) and average rates for the Nile Valley near Luxor (**k**) (this study; Extended Data Fig. 5). **l**, North African (10–28° N) palaeohydrological lake records as proxy for humidification and aridification of the Sahara and Sahel regions³⁴. **m**, Eastern Mediterranean Sapropel S1a/b⁴⁹. Egyptian cultural periods: Extended Data Table 5.

Holocene valley entrenchment with channel-bed incision and floodplain narrowing as found in our research (–11.5–4 ka) will have resulted in lower absolute flood levels during this time, assuming no changes in peak discharge. However, this same narrower floodplain will also have

made floods more turbulent with a higher amplitude, as water was funnelled through a narrower valley corridor (Fig. 3c,d). These flood dynamics would have occurred approximately between the Epipalaeolithic and the Old Kingdom/Middle Kingdom. The opposite effect will

have occurred when the floodplain expanded by aggradation thereafter (~4 ka–present) (Fig. 3e–g).

The profound environmental and geomorphological changes identified herein are also likely to have impacted the utilization of the Egyptian Nile Valley landscape through time. Particularly through the Old Kingdom, perhaps into the First Intermediate Period and maybe also the Middle Kingdom (Extended Data Table 5), the floodplain contraction associated with the formation of the T3 and T4 terraces between approximately 4.54 ± 0.42 ka and 4.09 ± 0.31 ka (Fig. 3c,d) would have progressively placed the high(er) terrace levels out of reach of the annual flood. As a result, these locations would not have annually received fertile Nile silts, and effective floodwater irrigation would not have been possible at these levels. Instead, these locations may have offered opportunities in terms of settlement or temple construction, being proximal to the river, but with a low risk of flooding (Fig. 3d–f).

In contrast, large-scale floodplain aggradation together with lateral floodplain expansion (Fig. 3e,f) took place after 4.09 ± 0.31 ka, from at least the Second Intermediate Period (Extended Data Table 5). These changes will not only have greatly enlarged the area of arable land in the Nile Valley near Luxor, but will also have created and sustained lush soils by regularly depositing fertile silts at rapid rates and in large quantities. The river was also less mobile from this time onwards compared with previous periods.

These insights into the dynamics of the Egyptian Nile Valley raise the question to what extent the stepwise shrinking of the active floodplain from 4.54 ± 0.42 ka onwards, and then its expansion after 4.09 ± 0.31 ka may have contributed to the concurrent success of the ancient Egyptian agricultural economy between the Old and New Kingdom periods (Extended Data Table 5)^{22,28}. Dating uncertainties preclude correlation with any specific events, but we would also argue strongly against the simple incorporation of any such correlations in grand causal links, especially given the fact that the environmental shifts were diachronous and may have had different expressions in different reaches of the river. Nonetheless, given the existence of major changes in floodplain reorganization, we argue for the necessary incorporation of the dynamic floodplain environment into archaeological change narratives, which must also include other endogenous and exogenous socio–political and economic factors.

Sedimentary system implications

In this study, we demonstrated that the sedimentary record of the Egyptian Nile near Luxor is a reflection of hydroclimatic changes and that storage and release of sediments from within the Nile Valley is impacted by a combination of upstream climatic and environmental factors and a downstream control exerted by sea-level change. This implies that downstream records might hold a mixed signal and could display a time delay with climatic perturbations in upstream regions. Our reconstructed fluvial evolution shows that the Nile Valley is not just a rigid conveyor belt for the transportation of water and sediments from upstream sources to downstream depocentres, but should be regarded as an important source-to-sink component itself.

Through our palaeo-environmental reconstruction near Luxor, we have shown that the single-channel Egyptian Nile of today is not analogous to the Nile system throughout much of the Holocene. For most of this time, the Egyptian Nile consisted of multiple mobile branches and did not comprise a single axial channel. Several co-existing active threads existed in a dynamic wandering-braided system from ~11.5 to 4 ka, and a number of less-dynamic straight channels were active between ~4 and 2 ka. The current single-thread, largely immobile Nile River, positioned centrally in its valley, only became established around 2,000 years ago. Importantly for archaeological prospection, our findings mean that large swaths of the buried stepped-terrace landscape remain undisturbed by fluvial erosion and thus potentially yield untouched archaeological traces of the specific age window between terrace abandonment and re-submergence by aggradation.

Hydroclimatic changes in the Nile Basin resulted in a rapidly changing fluvial system during the Holocene, with high sedimentation rates following earlier large-scale erosion, floodplain expansion following earlier contraction and a multi-channel system transforming into a single-thread system with avulsive behaviour. Such dynamics were not only the dominant drivers that shaped the Egyptian Nile Valley throughout the Holocene, but may have contributed to agro-economic dynamics in ancient Egyptian society. Ultimately, our results show that the classic view of ancient Egyptians cultivating a steadily aggrading floodplain^{22,28} is a great oversimplification of a much more complex fluvial system (Fig. 4h).

Online content

Any methods, additional references, Nature Portfolio reporting summaries, source data, extended data, supplementary information, acknowledgements, peer review information; details of author contributions and competing interests; and statements of data and code availability are available at <https://doi.org/10.1038/s41561-024-01451-z>.

References

1. Abdelsalam, M. G. The Nile's journey through space and time: a geological perspective. *Earth Sci. Rev.* **177**, 742–773 (2018).
2. Tierney, J. E. & deMenocal, P. B. Abrupt shifts in Horn of Africa hydroclimate since the Last Glacial Maximum. *Science* **342**, 843–846 (2013).
3. Shanahan, T. M. et al. The time-transgressive termination of the African Humid Period. *Nat. Geosci.* **8**, 140–144 (2015).
4. Castañeda, I. S. et al. Hydroclimate variability in the Nile River Basin during the past 28,000 years. *Earth Planet. Sci. Lett.* **438**, 47–56 (2016).
5. Tierney, J. E., Pausata, F. S. R. & deMenocal, P. B. Rainfall regimes of the Green Sahara. *Sci. Adv.* **3**, e1601503 (2017).
6. Larrasoña, J. C., Roberts, A. P. & Rohling, E. J. Dynamics of Green Sahara periods and their role in hominid evolution. *PLoS ONE* **8**, e76514 (2013).
7. Pausata, F. S. R. et al. The greenings of the Sahara: past changes and future implications. *One Earth* **2**, 235–250 (2020).
8. Stanley, D. J. & Warne, A. G. Nile Delta: recent geological evolution and human impact. *Science* **260**, 628–634 (1993).
9. Pennington, B. T., Sturt, F., Wilson, P., Rowland, J. & Brown, A. G. The fluvial evolution of the Holocene Nile Delta. *Quat. Sci. Rev.* **170**, 212–231 (2017).
10. Revel, M. et al. 100,000 years of African monsoon variability recorded in sediments of the Nile margin. *Quat. Sci. Rev.* **29**, 1342–1362 (2010).
11. Blanchet, C. L. et al. High- and low-latitude forcing of the Nile River regime during the Holocene inferred from laminated sediments of the Nile deep-sea fan. *Earth Planet. Sci. Lett.* **364**, 98–110 (2013).
12. Hennekam, R., Donders, T. H., Zwiep, K. & de Lange, G. J. Integral view of Holocene precipitation and vegetation changes in the Nile catchment area as inferred from its delta sediments. *Quat. Sci. Rev.* **130**, 189–199 (2015).
13. Revel, M. et al. 20,000 years of Nile River dynamics and environmental changes in the Nile catchment area as inferred from Nile upper continental slope sediments. *Quat. Sci. Rev.* **130**, 200–221 (2015).
14. Marks, L. et al. Holocene lake sediments from the Faiyum Oasis in Egypt: a record of environmental and climate change. *Boreas* **47**, 62–79 (2018).
15. Williams, M. A. J. et al. Late Quaternary floods and droughts in the Nile Valley, Sudan: new evidence from optically stimulated luminescence and AMS radiocarbon dating. *Quat. Sci. Rev.* **29**, 1116–1137 (2010).

16. Macklin, M. G. et al. Reach-scale river dynamics moderate the impact of rapid Holocene climate change on floodwater farming in the desert Nile. *Geology* **41**, 695–698 (2013).
17. Woodward, J. C. et al. Shifting sediment sources in the world's longest river: a strontium isotope record for the Holocene Nile. *Quat. Sci. Rev.* **130**, 124–140 (2015).
18. Bunbury, J. M., Graham, A. & Hunter, M. A. Stratigraphic landscape analysis: charting the Holocene movements of the Nile at Karnak through ancient Egyptian time. *Geoarchaeology* **23**, 351–373 (2008).
19. Hassan, F. A., Hamdan, M. A., Flower, R. J., Shallaly, N. A. & Ebrahim, E. Holocene alluvial history and archaeological significance of the Nile floodplain in the Saqqara–Memphis region, Egypt. *Quat. Sci. Rev.* **176**, 51–70 (2017).
20. Sheisha, H. et al. Nile waterscapes facilitated the construction of the Giza pyramids during the 3rd millennium BCE. *Proc. Natl Acad. Sci. USA* **119**, e2202530119 (2022).
21. Toonen, W. H. J. et al. The hydro-geomorphological setting of the Old Kingdom town of al-Ashmūnayn in the Egyptian Nile Valley. *Geoarchaeology* **37**, 267–283 (2022).
22. Butzer, K. W. *Early Hydraulic Civilization in Egypt: A Study in Cultural Ecology* (Univ. of Chicago Press, 1976).
23. Bunbury, J. M. *The Nile and Ancient Egypt: Changing Land- and Waterscapes from the Neolithic to the Roman Era* (Cambridge Univ. Press, 2019).
24. Said, R. *The River Nile: Geology, Hydrology and Utilization* (Pergamon, 1993).
25. Ullmann, M. in *Sacred Space and Sacred Function in Ancient Thebes* (eds Dorman, P. F. & Bryan, B. M.) 3–25 (Oriental Institute Univ. of Chicago, 2007).
26. Toonen, W. H. J. et al. Holocene fluvial history of the Nile's west bank at ancient Thebes, Luxor, Egypt, and its relation with cultural dynamics and basin-wide hydroclimatic variability. *Geoarchaeology* **33**, 273–290 (2018).
27. Allen, R. C. Agriculture and the origins of the state in Ancient Egypt. *Explor. Econ. Hist.* **34**, 135–154 (1997).
28. Hassan, F. A. The dynamics of a riverine civilization: a geoarchaeological perspective on the Nile Valley, Egypt. *World Archaeol.* **29**, 51–74 (1997).
29. Macklin, M. G. et al. A new model of river dynamics, hydroclimate change and human settlement in the Nile Valley derived from meta-analysis of the Holocene fluvial archive. *Quat. Sci. Rev.* **130**, 109–123 (2015).
30. Toonen, W. H. J. et al. Amenhotep III's mansion of millions of years in Thebes (Luxor, Egypt): submergence of high grounds by river floods and Nile sediments. *J. Archaeol. Sci. Rep.* **25**, 195–205 (2019).
31. *Topographical Map, Luxor Sheet, Scale 1:25,000* (Survey of Egypt, 1943).
32. Bini, M. et al. The 4.2 ka BP event in the Mediterranean region: an overview. *Clim. Past* **15**, 555–577 (2019).
33. Blum, M. D. & Törnqvist, T. E. Fluvial responses to climate and sea-level change: a review and look forward. *Sedimentology* **47**, 2–48 (2000).
34. Lézine, A.-M., Hély, C., Grenier, C., Braconnot, P. & Krinner, G. Sahara and Sahel vulnerability to climate changes, lessons from Holocene hydrological data. *Quat. Sci. Rev.* **30**, 3001–3012 (2011).
35. Berke, M. A. et al. Molecular records of climate variability and vegetation response since the Late Pleistocene in the Lake Victoria basin, East Africa. *Quat. Sci. Rev.* **55**, 59–74 (2012).
36. Jaeschke, A. et al. Holocene hydroclimatic variability and vegetation response in the Ethiopian Highlands (Lake Dendi). *Front. Earth Sci.* **8**, 585770 (2020).
37. Ménot, G. et al. Timing and stepwise transition of the African Humid Period from geochemical proxies in the Nile deep-sea sediments. *Quat. Sci. Rev.* **228**, 106071 (2020).
38. Krom, M. D., Stanley, J. D., Cliff, R. A. & Woodward, J. C. Nile River sediment fluctuations over the past 7000 yr and their key role in sapropel development. *Geology* **30**, 71–74 (2002).
39. Bastian, L. et al. Co-variations of climate and silicate weathering in the Nile Basin during the Late Pleistocene. *Quat. Sci. Rev.* **264**, 107012 (2021).
40. Blanchet, C. L., Frank, M. & Schouten, S. Asynchronous changes in vegetation, runoff and erosion in the Nile River watershed during the Holocene. *PLoS ONE* **9**, e115958 (2014).
41. Nyssen, J. et al. Human impact on the environment in the Ethiopian and Eritrean highlands—a state of the art. *Earth Sci. Rev.* **64**, 273–320 (2004).
42. Kuper, R. & Kröpelin, S. Climate-controlled Holocene occupation in the Sahara: motor of Africa's evolution. *Science* **313**, 803–807 (2006).
43. Zaki, A. S. et al. Did increased flooding during the African Humid Period force migration of modern humans from the Nile Valley? *Quat. Sci. Rev.* **272**, 107200 (2021).
44. Kröpelin, S. et al. Climate-driven ecosystem succession in the Sahara: the past 6000 years. *Science* **320**, 765–768 (2008).
45. Marriner, N., Flaux, C., Morhange, C. & Kaniewski, D. Nile Delta's sinking past: quantifiable links with Holocene compaction and climate-driven changes in sediment supply? *Geology* **40**, 1083–1086 (2012).
46. Seidlmayer, S. J., *Historische und moderne Nilstände: Untersuchungen zu den Pegelablesungen des Nils von der Frühzeit bis in die Gegenwart* (Achet Verlag Berlin, 2001).
47. Ditzler, C., Scheffe, K. & Monger, H. C. (eds) *Soil Survey Manual* (US Department of Agriculture, 2017).
48. Laskar, J. et al. A long-term numerical solution for the insolation quantities of the Earth. *Astron. Astrophys.* **428**, 261–285 (2004).
49. Hennekam, R., Jilbert, T., Schnetger, B. & de Lange, G. J. Solar forcing of Nile discharge and sapropel S1 formation in the early to middle Holocene eastern Mediterranean. *Paleoceanography* **29**, 343–356 (2014).

Publisher's note Springer Nature remains neutral with regard to jurisdictional claims in published maps and institutional affiliations.

Open Access This article is licensed under a Creative Commons Attribution 4.0 International License, which permits use, sharing, adaptation, distribution and reproduction in any medium or format, as long as you give appropriate credit to the original author(s) and the source, provide a link to the Creative Commons licence, and indicate if changes were made. The images or other third party material in this article are included in the article's Creative Commons licence, unless indicated otherwise in a credit line to the material. If material is not included in the article's Creative Commons licence and your intended use is not permitted by statutory regulation or exceeds the permitted use, you will need to obtain permission directly from the copyright holder. To view a copy of this licence, visit <http://creativecommons.org/licenses/by/4.0/>.

© The Author(s) 2024

¹Jebel Barkal Archaeological Project, Kelsey Museum of Archaeology, University of Michigan, Ann Arbor, MI, USA. ²Asian School of the Environment, Nanyang Technological University, Singapore, Singapore. ³Department of Archaeology and Ancient History, Uppsala University, Uppsala, Sweden. ⁴Earth and Climate, Vrije Universiteit Amsterdam, Amsterdam, The Netherlands. ⁵Egyptology Unit, Katholieke Universiteit Leuven, Leuven, Belgium. ⁶Geography and Environment, University of Southampton, Southampton, UK. ⁷Department of Geography, Winchester College, Winchester, UK. ⁸School of Geography and the Environment, University of Oxford, Oxford, UK. ⁹Department of Physical Geography, Utrecht University, Utrecht, The Netherlands. ¹⁰Archaeology, University of Southampton, Southampton, UK. ¹¹Department of Greece and Rome and Department of Egypt and Sudan, The British Museum, London, UK. ¹²Department of Natural Sciences, Manchester Metropolitan University, Manchester, UK. ¹³Fort Union National Monument, National Park Service, Watrous, NM, USA. ¹⁴Department of Egyptian Antiquities, Musée du Louvre, Paris, France. ¹⁵Independent researcher, Salisbury, UK. ¹⁶Department of Geology, Mansoura University, Mansoura, Egypt. ✉e-mail: angus.graham@arkeologi.uu.se

Methods

Sedimentary data and interpretation

Sedimentary information from 81 sediment cores retrieved by a combination of hand-operated Eijkelkamp augers and a gasoline-powered Cobra TT percussion corer was used to investigate the Nile's Holocene fluvial deposits in its valley near Luxor, Egypt. Sediment samples were studied in ~10 cm intervals and had their characteristics such as sedimentary texture (conforming to United States Department of Agriculture standards)⁴⁷, grain size, Munsell colour, degree of sorting, mica occurrence and rhizolith percentages logged on site. Boreholes reached to a mean depth of ~8 m—with many penetrating >10 m. Their spacing varied from ~20 to 200 m, depending on the heterogeneity of the subsurface. The cross section was strategically placed to span the entire valley, perpendicular to the main axis of the Nile Valley and the current river, while following governmental policies and regulatory procedures working in and around protected Egyptian Antiquities areas. Coring locations were recorded in UTM36N and the Survey of Egypt vertical datum using a Leica RTK-GNSS positioning system and subsequently stored together with the sedimentary logs for future reference (Supplementary Data 1). Subsequently, UTM36N coordinates were converted to degrees, minutes, seconds for publication purposes. Robust age information was provided through 48 quartz optically stimulated luminescence (OSL) ages, originating from 18 core sites spread across the Nile Valley (Fig. 1) strategically targeting the various sedimentary units (Fig. 2) for which OSL ages with 1σ standard deviation were calculated (Table 1; below provides further details on luminescence dating).

Luminescence dating procedures

Sampling and laboratory preparation. On the basis of the initial interpretation and reconstruction of the Holocene fluvial architecture in the Nile Valley by means of the newly constructed valley-wide cross section and after thorough inspection of the sedimentary logs, core-site locations were selected and revisited (within 1 m of their original borehole) to sample for luminescence dating; Extended Data Table 1 provides detailed sample locations and depths. Luminescence samples were collected using Eijkelkamp percussion coring equipment driven by a gasoline-powered Cobra TT hammer. For sampling, a metal core sampler (diameter 63 mm) with an exchangeable core catcher, lined with a dedicated black non-transparent PVC tube, was used to take undisturbed sediment samples of 50–100 cm in length. To prevent any possible disturbance, samples were preferentially taken from homogeneous intervals and sampling across bounding surfaces was avoided. After the sample was lifted to the surface and extruded from the sampler, the plastic liner containing the luminescence sample was cut to length (~25–30 cm), capped at both ends, labelled and wrapped in an opaque black plastic bag to avoid potential exposure to light. Sediment samples were subsequently transferred to the Geology Department of Mansoura University (Egypt) for initial sediment analyses and from there forwarded to the Oxford Luminescence Dating Laboratory at the University of Oxford (United Kingdom) for dating under a geological permit obtained by Mansoura University.

After transportation, the samples were opened and prepared under subdued orange-light conditions, with the light-exposed sample ends removed to avoid contamination. Sediment preparation followed standard laboratory procedures⁵⁰, with sediments treated using hydrochloric acid and hydrogen peroxide to remove any carbonate and organic material. All samples apart from those from cores AS107 and PC38 (that is, core sites VII and XV, respectively) were sieved and separated using sodium polytungstate heavy liquid density separation to isolate sand-sized grains of quartz (Extended Data Table 1 provides sample-specific grain-size ranges). These samples were chemically etched using hydrofluoric acid to remove the alpha-irradiated outer layer of the quartz grains. Sediments were loaded into aluminium single-grain discs (100 holes per disc arranged in a 10×10 array, with

a hole depth and diameter of 300 μm) for equivalent dose (D_e) measurement. Samples from cores AS107 and PC38 did not yield sufficient sand-sized grains for dating, and silt-sized grains of quartz were isolated using sieving and settling before chemical etching with fluoro-silicic acid. Prepared sediment (4–11 μm) was settled onto 9.7 mm aluminium discs for D_e measurement.

Equivalent dose rate measurement and calculation. OSL signals from quartz were measured using Risø TL/OSL DA-15 readers fitted with $^{90}\text{Sr}/^{90}\text{Y}$ beta sources with dose rates of c. 4 Gy min^{-1} . Ultraviolet luminescence signals were detected using a bi-alkali photomultiplier tube, through 7.5 mm U340 filters. Single-grain (SG) luminescence signals were stimulated with a 10 mW green (532 nm, Nd:YVO4) focused laser and multi-grain (MG) signals with a blue light-emitting diode array (470 nm, 28 mW cm^{-2}). The single aliquot regenerative dose (SAR) protocol^{51,52} (Extended Data Table 2) was used for D_e measurement. Following pre-heat plateau and dose recovery tests, a pre-heat of 220 °C and cut-heat of 160 °C for 10 s were used, and luminescence signals were measured at 125 °C for either 1 s (SG) or 40 s (MG). Single-grain D_e s were calculated from the signal derived from the first 0.1 s of measurement with a background from the final 0.2 s subtracted. Multi-grain D_e s were calculated from signal from the first 0.5 s, minus the background from the final 10 s. To assess suitability for dating, a suite of standard rejection criteria was applied to all luminescence signals. Signals were only included in final D_e calculation if they satisfied the following: (1) test dose signal was at least 3σ above background levels; (2) recycling ratios and (3) OSL IR (infrared) depletion ratios⁵³ were both within $\pm 10\%$ of unity (including uncertainties); and (4) recuperation was less than 5%. D_e determinations were made using either the central age model⁵⁴ or the finite mixture model⁵⁵.

Environmental dose rate determination. Environmental dose rates (\dot{D}) were calculated using DRAC dose rate and age calculator⁵⁶. Radionuclide concentrations were measured using inductively coupled plasma mass spectrometry and were converted into infinite-matrix \dot{D} s using the conversion factors of Guérin et al.⁵⁷. Adjustments for attenuation by grain size and chemical etching were made using the factors of Guérin et al.⁵⁷ and Bell⁵⁸, respectively, and for the fine-grain quartz samples (cores AS107 and PC38), an additive a -value of 0.038 ± 0.02 (ref. 59) was used to calculate the Alpha \dot{D} . To correct for attenuation by water in the sediment matrix, the factors of Aitken and Xie⁶⁰ and Zimmerman⁶¹ were used, and sample-specific water content values (Extended Data Table 3) were chosen to reflect groundwater development during the burial history of the samples. Cosmic dose rate determination was based upon sample geographic location and depth, calculated following Prescott and Hutton⁶². Dose rate data are provided in Extended Data Table 3.

Luminescence dating results

The use of the OSL signal for dating. Combined pre-heat dose recovery and dose recovery tests were used to test the suitability of the SAR protocol for D_e measurement. For combined pre-heat dose recovery tests, three samples were selected, and the ability of the SAR protocol (Extended Data Table 2) to recover a known dose was tested while varying the pre-heat temperature (step 2, Extended Data Table 2) at 20 °C intervals between 200 °C and 260 °C. Data are summarized in Extended Data Table 4, and recovery of the administered dose to within $\pm 10\%$ of unity (frequently $\pm 5\%$) indicate that these samples are not sensitive to the selected pre-heat temperature across the range 200–260 °C (for example, Extended Data Fig. 1). A pre-heat temperature of 220 °C was selected and further tested with MG and SG dose recovery experiments on a larger number of samples. For all experiments, the administered dose (ranging between 5 and 15 Gy) was successfully recorded to within $\pm 10\%$ of unit taking into account uncertainties (Extended Data Fig. 2a,b and Extended Data Table 4). Successful dose recovery experiments, across SG and MG scales,

demonstrates the suitability of the SAR protocol for obtaining D_e determinations for these sediments.

Quartz OSL signals measured from this suite of samples are generally sensitive (bright) and high yielding (Extended Data Fig. 3a,b and Extended Data Table 1). OSL signals were clearly discernible from the reader background and were observed to decay rapidly to near background levels (Extended Data Fig. 3a,b), suggesting the signal was fast-component dominated, and the application of the fast ratio⁶³ to MG OSL signals was used to confirm this. Sediments from this suite of samples were reasonably high yielding, with the number of grains providing a discernible luminescence signal and satisfying all rejection criteria being typically 4–5%, ranging between 1.8 and 8.5% for most samples. For sample AS145-1, the extremely low yield of sand-sized grains for dating resulted in the use of a 90–210 μm grain-size range for dating and probably multiple grains per hole, hence the higher-than-average yield (26%). Dating of this sample should be considered as very small aliquot dating rather than single grain.

Overdispersion (σ_d) for the suite of SG samples varied between 11.1 and 33.5%. Example D_e distributions are shown in Extended Data Fig. 4a–c (samples AS87-3, AS82-3 and AS75-4, respectively), with two additional higher σ_d values of 106.2% (sample AS89-1; Supplementary Data 1) and 130.8% (sample AS118-1; Extended Data Fig. 4e). Sample AS89-1 has a low D_e of 0.39 ± 0.07 Gy, and with σ_d calculated as a percentage of D_e , this gives rise to the inflated σ_d . Sample AS118-1 is more interesting, showing a clear bimodal distribution (Extended Data Fig. 4e), with a younger component giving a D_e of 9.63 ± 2.15 Gy and a higher dose component exceeding 80 Gy, made up of a combination of near-saturated and saturated D_e s (where $D_e > 2D_0$ or a non-intercepting D_e). Re-examination of the sediment log shows sample AS118-1 contains high proportions of degraded sandstone, which most likely is the cause for these (near-) saturated D_e values. These two samples aside, overdispersion for this suite of single-grain samples is however low. For the multi-grain samples, nine of the ten samples had σ_d of less than 1%, with only sample AS107-3 having a higher σ_d of 11.2%, caused predominantly by the presence of one high D_e value (Extended Data Fig. 4f), the cause of which we cannot yet confirm. Overall, however, given the low calculated σ_d values, we suggest this is a suite of samples, which, for the most part, are not adversely impacted by factors such as heterogeneous bleaching, microdosimetry or post-depositional mixing, which can often lead to complications in age calculation. Therefore, the central age model of Galbraith et al.⁵⁴ has been used for final D_e determination, apart from samples AS89-1 and AS118-1 where the finite mixture model⁵⁵ was used to isolate the low dose component.

Luminescence ages

In total, 38 quartz SG OSL ages from sand-sized sediments and ten quartz MG OSL ages from fine-grained sediments have been calculated. All samples date to the Holocene and are associated with uncertainties of typically ± 7 –8% for SG ages and ± 6 –7% for MG ages. After careful inspection of the sedimentological and stratigraphic positions of the entire OSL dataset and re-examination of the sedimentary logs, four samples of the total set of 48 samples (that is, AS107-9, AS118-1, AS119-1 and AS141-1) were not included in the median age calculations using the probability density function method (below). Sample AS118-1 is found to contain high proportions of (degraded) yellow sandstone, which most likely is the cause of (near-)saturated D_e values and a D_e distribution comprised of multiple distinctive components (Extended Data Fig. 4e). The presence of sandstone, which is allochthonous in origin in the floodplain, more importantly points to a very high probability of anthropogenic disturbance of the sediments at this location. Similar probable disturbance also excludes sample AS119-1, which is found at a similar position at the top of the T3 terrace, where it neighbours AS118-1. Sample AS107-9 is considered disturbed as well, albeit by forces of nature, as the top of the T4 terrace appears to have been reworked after deposition by

fluvial activity, apparently during the initial stages of CB1 channel belt formation, overtopping the terrace during flood conditions and reworking its deposits. Sample AS141-1 is considered disturbed by natural forces too, as the presence of clay balls just beneath the sample and the pale-coloured sediments just above the sample indicate fluvial activity and reworking of the original terrace deposits by wadi plain run-off processes during the African Humid Period^{3,5}. Hence, this sample was excluded from median age calculation.

Subsequently, the median age and 1σ standard deviation were calculated for each identified geogenetic unit (Table 1) by stacking the individual Gaussian distribution curves of accepted OSL dating results within each unit. This approach weighs clustering of OSL ages in assigning age ranges, leaving the age of the particular unit less sensitive to outliers^{64,65}. Table 1 provides all calculated median age results per unit.

Data availability

The datasets generated and analysed for this study are available in the main text, Methods, Extended Data and/or Supplementary Data 1. In addition, our sediment core dataset is also openly available via Zenodo at <https://doi.org/10.5281/zenodo.10813774> (ref. 66).

References

- Wintle, A. G. Luminescence dating: laboratory procedures and protocols. *Radiat. Meas.* **27**, 769–817 (1997).
- Murray, A. S. & Wintle, A. G. Luminescence dating of quartz using an improved single-aliquot regenerative-dose protocol. *Radiat. Meas.* **32**, 57–73 (2000).
- Wintle, A. G. & Murray, A. S. A review of quartz optically stimulated luminescence characteristics and their relevance in single-aliquot regeneration dating protocols. *Radiat. Meas.* **41**, 369–391 (2006).
- Duller, G. A. T. Distinguishing quartz and feldspar in single grain luminescence measurements. *Radiat. Meas.* **37**, 161–165 (2003).
- Galbraith, R. F., Roberts, R. G., Laslett, G. M., Yoshida, H. & Olley, J. M. Optical dating of single and multiple grains of quartz from Jinmium rock shelter, northern Australia: part I, experimental design and statistical models. *Archaeometry* **2**, 339–364 (1999).
- Galbraith, R. F. & Green, P. F. Estimating the component ages in a finite mixture. *Int. J. Radiat. Appl. Instrum. Part D* **117**, 197–206 (1990).
- Durcan, J. A., King, G. E. & Duller, G. A. T. DRAC: dose rate and age calculator for trapped charge dating. *Quat. Geochron.* **28**, 54–61 (2015).
- Guérin, G., Mercier, N., Nathan, R., Adamiec, G. & Lefrais, Y. On the use of the infinite matrix assumption and associated concepts: a critical review. *Radiat. Meas.* **47**, 778–785 (2012).
- Bell, W. T. Attenuation factors for the absorbed radiation dose in quartz inclusions for thermoluminescence dating. *Ancient TL* **8**, 2–13 (1979).
- Rees-Jones, J. Optical dating of young sediments using fine-grained quartz. *Ancient TL* **13**, 9–14 (1995).
- Aitken, M. J. & Xie, J. Moisture correction for annual gamma dose. *Ancient TL* **8**, 6–9 (1990).
- Zimmerman, D. W. Thermoluminescent dating using fine grains from pottery. *Archaeometry* **13**, 29–52 (1971).
- Prescott, J. R. & Hutton, J. T. Cosmic ray contributions to dose rates for luminescence and ESR dating: large depths and long-term time variations. *Radiat. Meas.* **23**, 497–500 (1994).
- Durcan, J. A. & Duller, G. A. T. The fast ratio: a rapid measure for testing the dominance of the fast component in the initial OSL signal from quartz. *Radiat. Meas.* **46**, 1065–1072 (2011).
- Busschers, F. S. et al. Late Pleistocene evolution of the Rhine–Meuse system in the southern North Sea basin: imprints of climate change, sea-level oscillation and glacio-isostasy. *Quat. Sci. Rev.* **26**, 3216–3248 (2007).

65. Peeters, J. et al. Sedimentary architecture and chronostratigraphy of a late Quaternary incised-valley fill: a case study of the late Middle and Late Pleistocene Rhine system in the Netherlands. *Quat. Sci. Rev.* **131**, 211–236 (2016).
66. Peeters, J. et al. Sediment core dataset for ‘Shift away from Nile incision at Luxor ~4000 years ago impacted ancient Egyptian landscapes’. *Zenodo* <https://doi.org/10.5281/zenodo.10813774> (2024).
67. Zeeden, C., Dietze, M. & Kreuzer, S. Discriminating luminescence age uncertainty composition for a robust Bayesian modelling. *Quat. Geochronol.* **43**, 30–39 (2018).
68. Wensinck, A. J., et al. in *Encyclopaedia of Islam* 2nd edn (eds Bearman, P. et al.) Vol. 7, 146–186 (Brill, 2012).
69. Lloyd, A. B. (ed.) *A Companion to Ancient Egypt* Vol. 1 (Wiley-Blackwell, 2010).
70. Hornung, E., Krauss, R. & Warburton, D. A. (eds) *Ancient Egyptian Chronology. Handbook of Oriental Studies* Vol. 83 (Brill, 2006).
71. Payraudeau, F. *L'Égypte et la Vallée du Nil. Tome 3: Les époques Tardives* (Presses Univ. de France, 2020).
72. Dee, M. et al. An absolute chronology for early Egypt using radiocarbon dating and Bayesian statistical modelling. *Proc. R. Soc. A.* **469**, 20130395 (2013).
73. Tassie, G. J. *Prehistoric Egypt: Socioeconomic Change in North-east Africa from the Last Glacial Maximum to the Neolithic, 24,000 to 6,000 cal BP* (Golden House Publications, 2014).

Acknowledgements

We thank all contributors to the Theban Harbours and Waterscapes Survey (THaWS). We are greatly indebted to the Egyptian Ministry of Tourism and Antiquities, the Farouk family, our local team members and landowners for their efforts and support in the field and beyond. THaWS functioned under the auspices of the Egypt Exploration Society (London, United Kingdom). The views expressed in the article do not necessarily represent the views of the National Park Service or the United States.

Author contributions

The research was conceived by J.P., A.G., W.H.J.T. and B.T.P. Sample collection was performed by all authors, with formal analyses performed by J.P., W.H.J.T., B.T.P., J.A.D., T.G.W., K.A., A.M.-B. and M.M. The data were curated by J.P., A.G., W.H.J.T., B.T.P. and J.A.D. Responsible for funding acquisition and project administration was A.G. The first draft of the manuscript was written by J.P. and J.A.D. (luminescence dating), with further editing and input from all authors.

Funding

THaWS is supported by the Knut and Alice Wallenberg Foundation and Uppsala University through principal investigator A.G. (Wallenberg Academy Fellow, 2014–20). Open access funding provided by Uppsala University.

Competing interests

The authors declare no competing interests.

Additional information

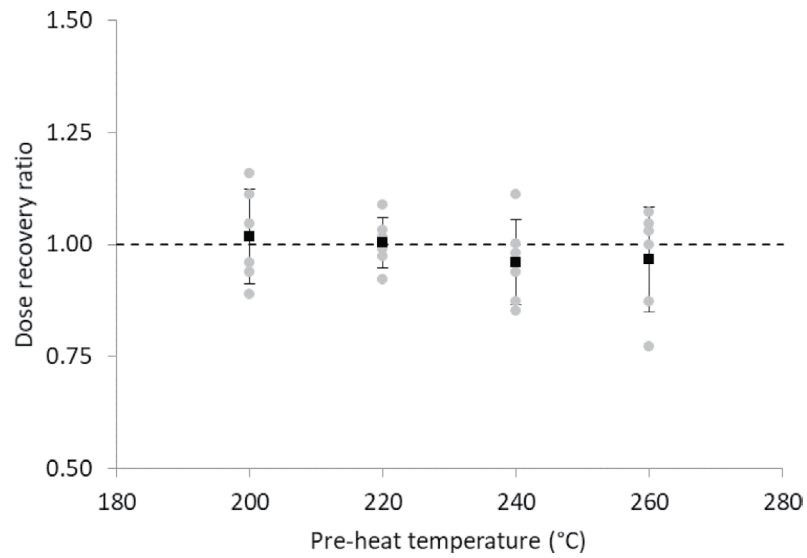
Extended data is available for this paper at <https://doi.org/10.1038/s41561-024-01451-z>.

Supplementary information The online version contains supplementary material available at <https://doi.org/10.1038/s41561-024-01451-z>.

Correspondence and requests for materials should be addressed to Angus Graham.

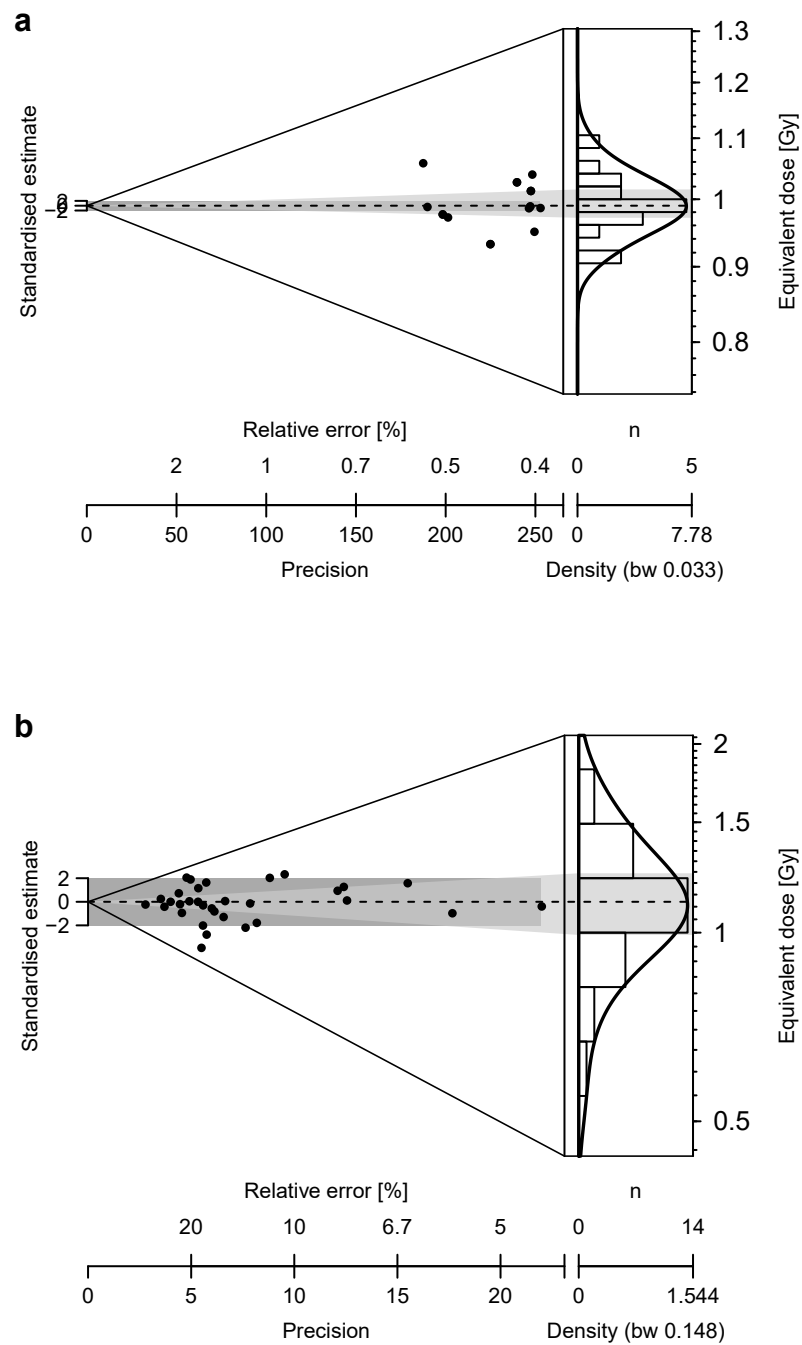
Peer review information *Nature Geoscience* thanks Cecile Blanchet, Eva Lange-Athinodorou and the other, anonymous, reviewer(s) for their contribution to the peer review of this work. Primary Handling Editors: James Super and Tamara Goldin, in collaboration with the *Nature Geoscience* team.

Reprints and permissions information is available at www.nature.com/reprints.



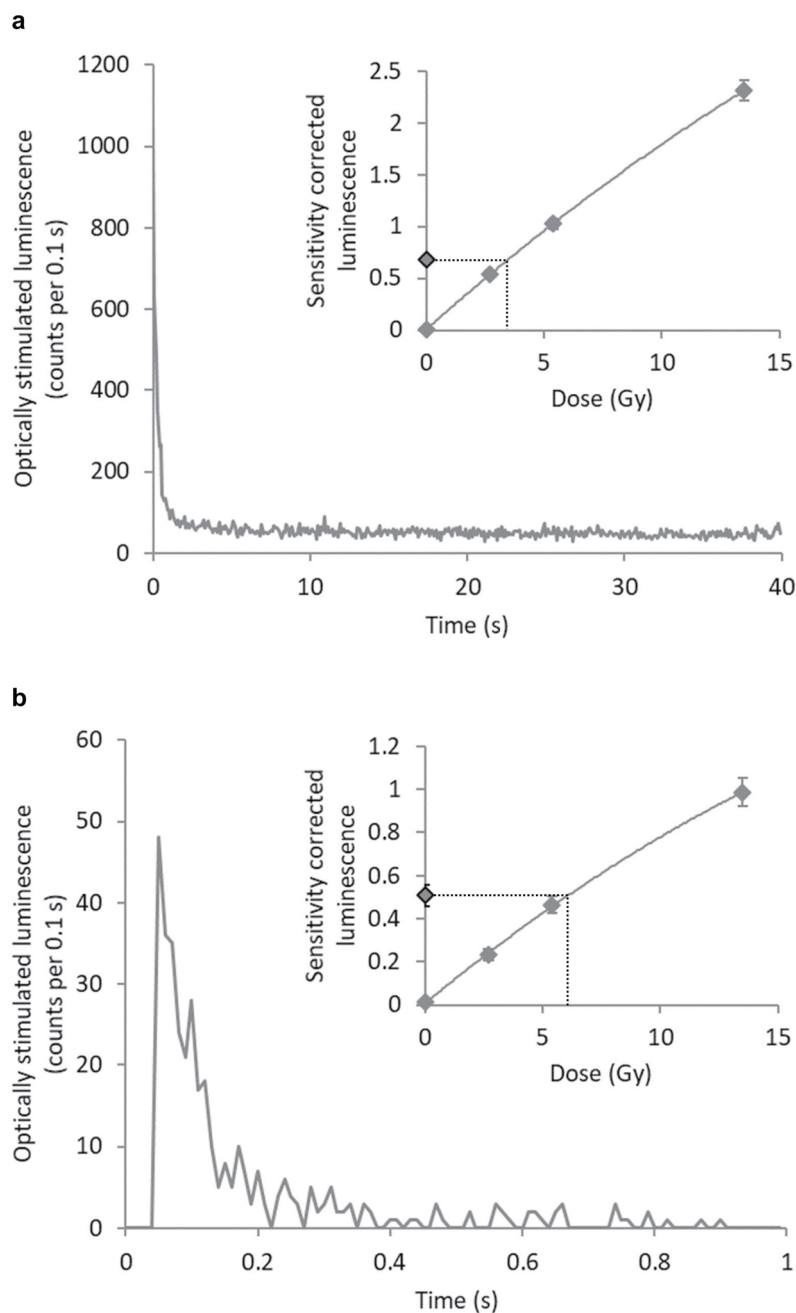
Extended Data Fig. 1 | Combined pre-heat and dose recovery data. Example for sample AS73-1 from core site III. Six small aliquots of this sample were measured using the SAR cycle with varying pre-heat temperatures across the

range of 200–260 °C. A dose of 5 Gy was recovered, and the ratio between this administered dose and the recovered dose are plotted for individual aliquots (grey symbols) along with the average and standard deviation (black symbols).



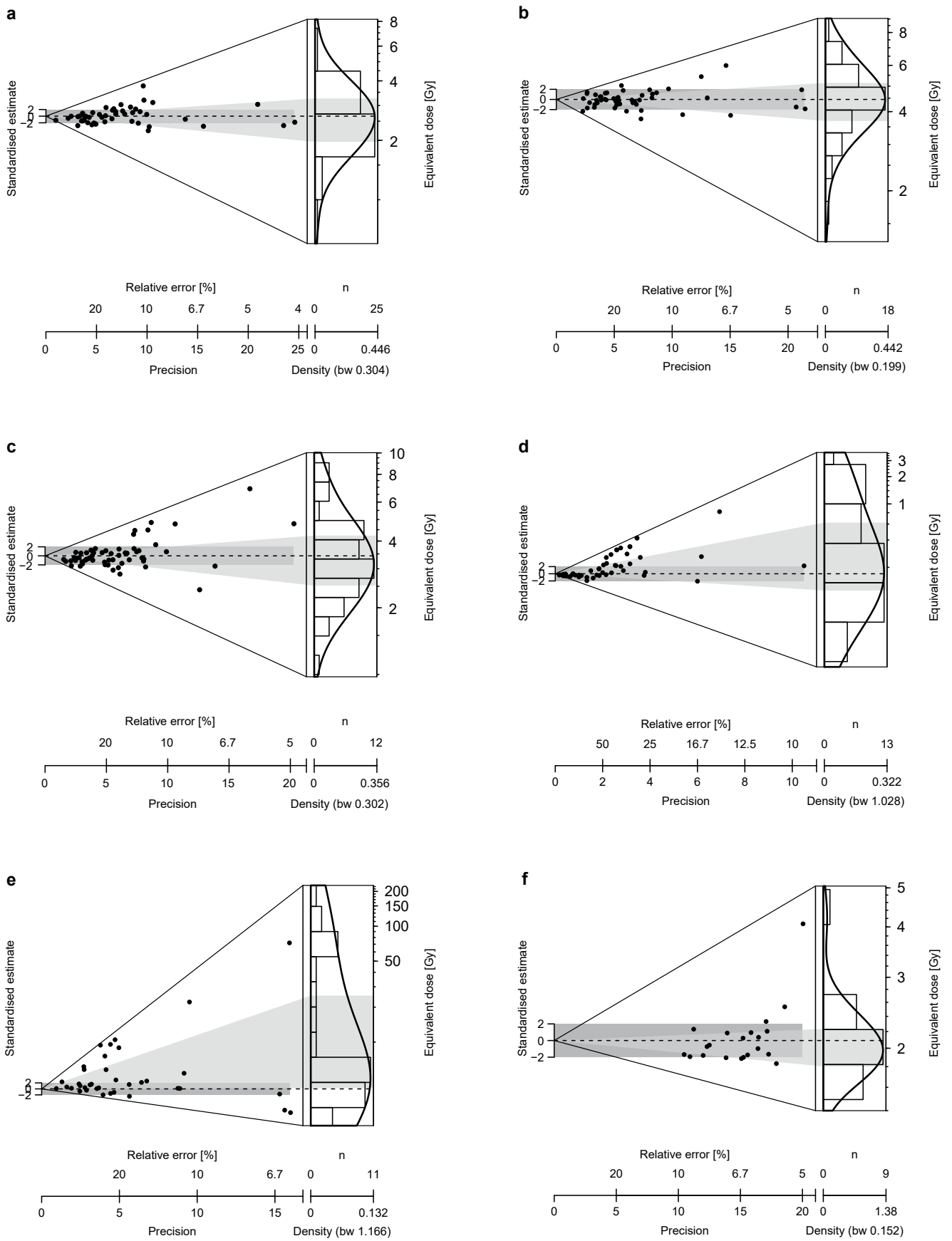
Extended Data Fig. 2 | Dose recovery abanico plots. Showing data for (a) small aliquots ($n = 11$) and (b) single grains of sample AS73-1 ($n = 32$) from core site III. A dose of 5 Gy was recovered in both experiments, and the ratio between this

administered dose and the recovered dose is plotted. The dashed line shows the mean recovered dose, with the dark grey band indicating $\pm 2\sigma$ of this value. Also shown by the light grey shading is the quartile range.



Extended Data Fig. 3 | Example OSL signals and the corresponding dose response curve (inset). In (a) the OSL signal from a single multi-grain disc of sample AS107-4 (core site VII) is shown. The calculated D_e of 3.47 ± 0.16 Gy is indicated by the dotted line on the dose response curve. In (b) the OSL signal

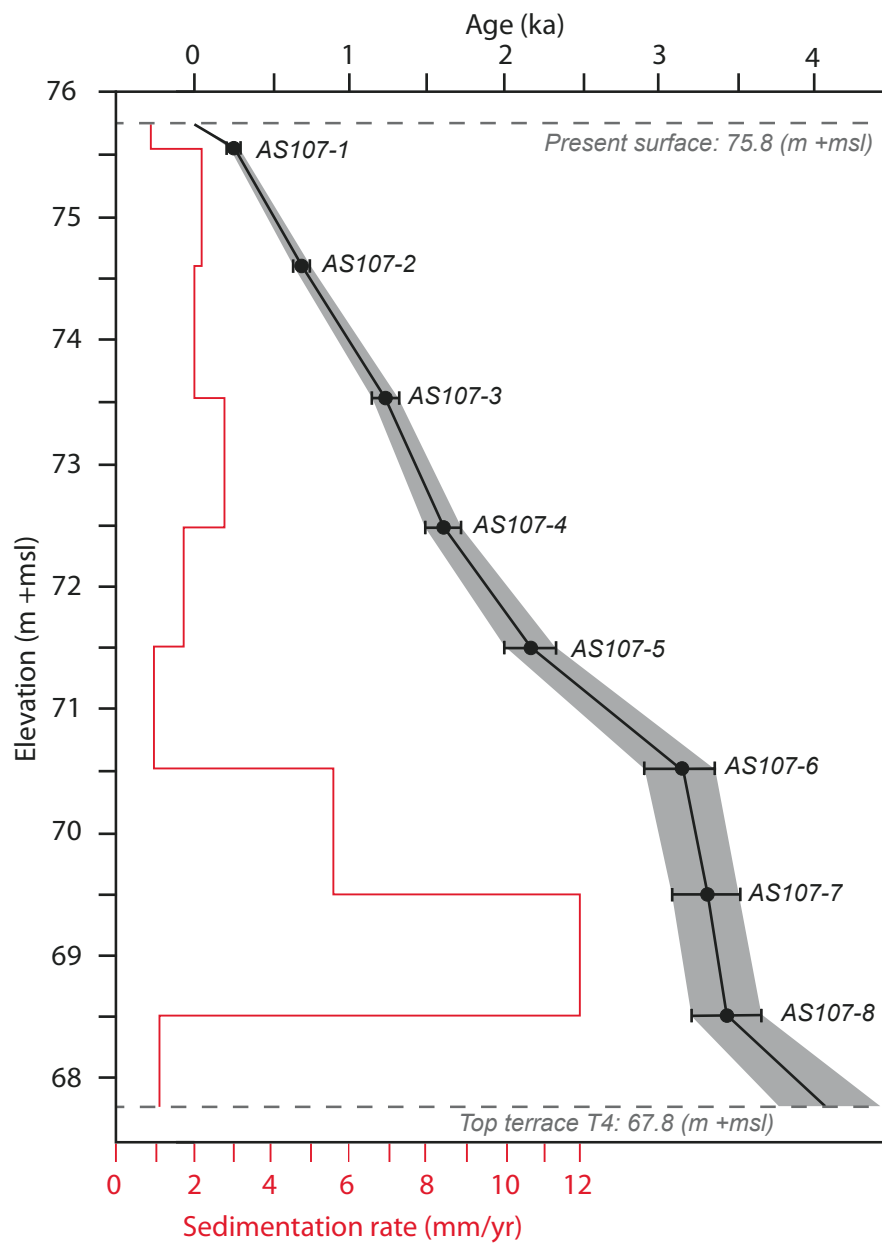
from a single grain of sample AS87-3 (core site IV) (D_e 6.17 ± 0.66 Gy) and the dose response curve are shown. Uncertainties have been calculated by combining and propagating in quadrature systematic and random sources of uncertainty.



Extended Data Fig. 4 | See next page for caption.

Extended Data Fig. 4 | D_e distribution abanico plots. Showing examples of (a) AS82-3 ($n = 49$), (b) AS87-3 ($n = 50$), (c) AS75-4 ($n = 57$), (d) AS89-1 ($n = 50$), (e) AS118-1 ($n = 74$), as well as 17 datapoints which have not been plotted for this sample due to the saturation of OSL signals, which provided infinite D_e

determinations), and (f) AS107-3 ($n = 21$). Sample D_e values were calculated using either the central age model (a-d, f) or the finite mixture model (e). Dashed lines show the calculated D_e , with the dark grey band indicating $\pm 2\sigma$ of this value. The quartile range is shown by the light grey shading.



Extended Data Fig. 5 | Age-depth model for core-site VII/AS107. The solid black line shows the modelled Bayesian age-depth-relationship⁶⁷; the 95% confidence interval is indicated with the grey band. OSL ages ($n = 8$) are shown with their 1σ SD. The stepped red line shows the average sedimentation rate (mm/yr).

Extended Data Table 1 | Equivalent dose (D_e) and age data

Core site / sample number	Sample depth (m below surface)	Grain size (μm)	Measured signal (single / multi grain)	Accepted (measured) grains/discs (n)	Over-dispersion (%)	Age Model	D_e (Gy)	\dot{D} ($\text{Gy}\cdot\text{ka}^{-1}$)	Age (ka)
I / AS181: 25°43'10"N, 32°36'12"E; 76.6 m.a.s.l.									
AS181-1	8.41–8.66	180–210	SG	63 (1100)	25.7±3.9	CAM	7.57±0.32	1.51±0.09	5.03±0.37
AS181-2	8.66–8.91	180–210	SG	52 (700)	14.4±4.4	CAM	6.44±0.23	1.43±0.09	4.52±0.32
II / AS71: 25°43'04"N, 32°36'21"E; 75.8 m.a.s.l.									
AS71-1	9.66–9.79	180–210	SG	53 (1000)	17.3±4.3	CAM	3.57±0.14	0.83±0.05	4.33±0.32
AS71-2	9.91–10.04	180–210	SG	62 (1200)	22.8±4.0	CAM	2.93±0.12	0.76±0.05	3.84±0.30
III / AS73: 25°42'58"N, 32°36'31"E; 75.6 m.a.s.l.									
AS73-1	7.29–7.44	180–210	SG	51 (1200)	27.3±4.7	CAM	3.70±0.19	1.22±0.08	3.04±0.25
AS73-2	7.59–7.74	180–210	SG	53 (1200)	22.9±4.6	CAM	4.36±0.20	1.32±0.09	3.29±0.27
IV / AS87: 25°42'57"N, 32°36'34"E; 75.5 m.a.s.l.									
AS87-1	4.34–4.64	180–250	SG	48 (1300)	28.8±4.6	CAM	3.76±0.20	1.33±0.08	2.84±0.22
AS87-2	6.14–6.29	180–210	SG	69 (1000)	26.6±3.6	CAM	4.69±0.19	1.27±0.07	3.69±0.26
AS87-3	6.44–6.59	180–250	SG	50 (1600)	11.1±5.5	CAM	4.45±0.16	1.31±0.09	3.39±0.25
V / AS75: 25°42'53"N, 32°36'41"E; 75.7 m.a.s.l.									
AS75-1	4.18–4.47	150–210	SG	62 (2200)	30.4±4.6	CAM	4.90±0.25	1.35±0.09	3.64±0.30
AS75-2	6.02–6.32	180–210	SG	47 (1200)	29.0±5.1	CAM	4.32±0.24	1.30±0.08	3.32±0.27
AS75-3	8.22–8.37	180–210	SG	64 (1500)	25.9±4.2	CAM	3.64±0.16	1.00±0.07	3.64±0.30
AS75-4	8.52–8.67	180–210	SG	57 (1400)	33.5±5.0	CAM	3.43±0.19	1.06±0.08	3.23±0.29
VI / AS76: 25°42'49"N, 32°36'47"E; 75.8 m.a.s.l.									
AS76-1	5.99–6.12	150–180	SG	71 (1000)	27.3±3.8	CAM	3.34±0.14	1.25±0.08	2.66±0.20
AS76-2	6.24–6.37	150–180	SG	57 (1000)	26.2±4.0	CAM	3.81±0.17	1.27±0.08	3.00±0.22
VII / AS107: 25°42'49"N, 32°36'50"E; 75.8 m.a.s.l.									
AS107-1	0.18–0.28	4–11	MG	25 (25)	0.0±0.0	CAM	0.52±0.02	1.94±0.11	0.27±0.02
AS107-2	1.18–1.28	4–11	MG	25 (25)	0.0±0.0	CAM	1.33±0.04	1.85±0.72	0.72±0.05
AS107-3	2.23–2.33	4–11	MG	21 (25)	11.2±5.5	CAM	2.09±0.09	1.69±0.10	1.24±0.09
AS107-4	3.23–3.33	4–11	MG	23 (25)	0.0±0.0	CAM	2.63±0.09	1.64±0.10	1.60±0.11
AS107-5	4.23–4.33	4–11	MG	24 (25)	0.1±0.1	CAM	3.46±0.11	1.58±0.09	2.18±0.15
AS107-6	5.23–5.33	4–11	MG	25 (25)	0.0±0.0	CAM	5.03±0.16	1.59±0.09	3.16±0.21
AS107-7	6.23–6.33	4–11	MG	24 (25)	0.0±0.0	CAM	5.00±0.16	1.50±0.09	3.34±0.22
AS107-8	7.18–7.31	4–11	MG	25 (25)	0.0±0.0	CAM	4.92±0.15	1.44±0.09	3.42±0.23
AS107-9	8.18–8.28	150–250	SG	50 (1100)	23.2±5.0	CAM	3.37±0.17	1.16±0.08	2.90±0.25
VIII / AS77: 25°42'46"N, 32°36'54"E; 76.0 m.a.s.l.									
AS77-1	9.40–9.65	90–210	SG	68 (1200)	31.9±4.6	CAM	3.55±0.18	1.43±0.09	2.49±0.20
AS77-2	9.95–10.20	180–120	SG	52 (1400)	24.6±4.7	CAM	3.43±0.17	1.31±0.08	2.62±0.21
IX / AS145: 25°42'38"N, 32°37'12"E; 76.1 m.a.s.l.									
AS145-1	6.59–6.74	90–210	SG	266 (1000)	26.9±0.1	CAM	3.51±0.10	1.29±0.08	2.73±0.19
AS145-2	7.19–7.34	90–250	SG	65 (1000)	18.9±4.1	CAM	4.14±0.16	1.25±0.07	3.31±0.23
X / AS82: 25°42'34"N, 32°37'23"E; 76.2 m.a.s.l.									
AS82-1	5.32–5.45	180–250	SG	51 (1200)	19.3±4.0	CAM	4.40±0.17	1.29±0.08	3.42±0.26
AS82-2	5.57–5.70	150–250	SG	52 (800)	30.4±4.6	CAM	3.47±0.18	1.32±0.08	2.62±0.21
AS82-3	9.02–9.15	180–210	SG	49 (1000)	24.2±4.6	CAM	2.65±0.13	0.89±0.06	2.99±0.24
AS82-4	9.27–9.40	180–210	SG	56 (1000)	22.1±4.4	CAM	2.69±0.12	1.18±0.08	2.27±0.18
XI / AS89: 25°42'19"N, 32°37'53"E; 76.3 m.a.s.l.									
AS89-1	1.86–1.99	180–210	SG	50 (2800)	106.2±14.4	FMM	0.17±0.02	1.50±0.08	0.11±0.01
XII / PC32: 25°43'02"N, 32°39'52"E; 76.7 m.a.s.l.									
PC32-1	8.19–8.32	150–210	SG	98 (1400)	30.4±3.5	CAM	2.03±0.08	1.29±0.08	1.57±0.12
PC32-2	8.44–8.57	180–210	SG	51 (1000)	45.2±6.1	CAM	1.86±0.14	1.23±0.08	1.52±0.15
XIII / AS118: 25°42'43"N, 32°40'22"E; 75.2 m.a.s.l.									
AS118-1	3.20–3.35	180–210	SG	74 (1800)	130.8±16.3	FMM	3.94±0.20	1.27±0.07	3.10±0.24
AS118-2	5.20–5.35	180–210	SG	52 (1300)	32.4±4.8	CAM	3.67±0.21	1.09±0.07	3.38±0.30
XIV / AS119: 25°42'40"N, 32°40'26"E; 75.2 m.a.s.l.									
AS119-1	4.69–4.82	180–210	SG	52 (1200)	24.4±4.8	CAM	3.44±0.17	1.18±0.09	2.92±0.26
AS119-2	4.94–5.07	180–210	SG	55 (1400)	34.6±5.1	CAM	3.45±0.20	0.78±0.08	4.45±0.52
XV / PC38: 25°42'38"N, 32°40'30"E; 75.2 m.a.s.l.									
PC38-1	7.20–7.30	4–11	MG	25 (25)	0.0±0.0	CAM	5.21±0.16	1.39±0.09	3.76±0.26
PC38-2	7.45–7.55	4–11	MG	25 (25)	0.0±0.0	CAM	5.41±0.17	1.34±0.08	4.03±0.28
XVI / AS131: 25°42'06"N, 32°41'04"E; 75.3 m.a.s.l.									
AS131-1	4.80–4.95	180–210	SG	47 (900)	20.7±4.3	CAM	4.56±0.20	1.04±0.06	4.37±0.31
AS131-2	5.10–5.25	180–210	SG	57 (1300)	16.4±4.3	CAM	4.29±0.16	0.78±0.05	5.50±0.40
XVII / AS136: 25°41'31"N, 32°41'46"E; 75.8 m.a.s.l.									
AS136-1	1.08–1.21	180–210	SG	56 (1000)	32.1±4.6	CAM	7.99±0.43	1.02±0.06	7.83±0.62
AS136-2	2.41–2.53	180–210	SG	75 (1000)	12.6±4.1	CAM	9.52±0.29	0.97±0.06	9.87±0.70
XVIII / AS141: 25°41'13"N, 32°42'10"E; 79.0 m.a.s.l.									
AS141-1	1.32–1.47	180–210	SG	53 (1300)	26.4±4.5	CAM	9.45±0.46	1.22±0.07	7.72±0.56
AS141-2	3.62–3.77	180–210	SG	53 (1600)	24.8±4.6	CAM	13.60±0.65	1.33±0.09	10.21±0.83
AS141-3	4.27–4.42	180–210	SG	55 (1500)	25.0±4.4	CAM	12.95±0.60	1.50±0.09	8.62±0.67

Note: Coordinates are in degrees, minutes, seconds (latitude/longitude); surface elevation is in meters above sea level (m.a.s.l.).

Extended Data Table 2 | Single Aliquot Regenerative dose (SAR) protocol

Step	Treatment
1	Dose
2	Pre-heat at 220°C for 10 s
3	OSL at 125°C for 1 s (single grain) OSL at 125°C for 40 s (multi-grain)
4	Test dose
5	Cut-heat at 160°C for 10 s
6	IRSL at 50°C for 50 s
7	OSL at 125°C for 1 s (single grain) OSL at 125°C for 40 s (multi-grain)

Note: The IRSL measurement in step 6 was applied to the final SAR cycle only in order to check for signal contamination.

Extended Data Table 3 | Dose rate (\dot{D}) data

Core site / sample number	Grain size (μm)	Water Content (%)	U (ppm)	Th (ppm)	K (%)	Alpha \dot{D} ($\text{Gy}\cdot\text{ka}^{-1}$)	Beta \dot{D} ($\text{Gy}\cdot\text{ka}^{-1}$)	Gamma \dot{D} ($\text{Gy}\cdot\text{ka}^{-1}$)	Cosmic \dot{D} ($\text{Gy}\cdot\text{ka}^{-1}$)	Environmental \dot{D} ($\text{Gy}\cdot\text{ka}^{-1}$)
I / AS181: 25°43'10"N, 32°36'12"E; 76.6 m.a.s.l.										
AS181-1	180–210	20±5	1.39±0.14	5.48±0.55	1.09±0.11	0.00±0.00	0.87±0.08	0.56±0.04	0.08±0.01	1.51±0.09
AS181-2	180–210	20±5	1.37±0.14	4.74±0.47	1.05±0.11	0.00±0.00	0.83±0.08	0.52±0.04	0.08±0.01	1.43±0.09
II / AS71: 25°43'04"N, 32°36'21"E; 75.8 m.a.s.l.										
AS71-1	180–210	25±5	0.48±0.05	1.92±0.19	0.75±0.07	0.00±0.00	0.50±0.05	0.26±0.02	0.07±0.01	0.83±0.05
AS71-2	180–210	25±5	0.42±0.04	1.43±0.14	0.72±0.07	0.00±0.00	0.47±0.05	0.23±0.02	0.07±0.01	0.76±0.05
III / AS73: 25°42'58"N, 32°36'31"E; 75.6 m.a.s.l.										
AS73-1	180–210	25±5	0.82±0.08	2.32±0.23	1.14±0.11	0.00±0.00	0.75±0.07	0.38±0.03	0.09±0.01	1.22±0.08
AS73-2	180–210	25±5	0.69±0.07	2.37±0.24	1.31±0.13	0.00±0.00	0.84±0.08	0.40±0.03	0.08±0.01	1.32±0.09
IV / AS87: 25°42'57"N, 32°36'34"E; 75.5 m.a.s.l.										
AS87-1	180–250	20±5	1.36±0.14	4.50±0.45	0.90±0.09	0.00±0.00	0.73±0.07	0.48±0.04	0.12±0.01	1.33±0.08
AS87-2	180–210	20±5	1.03±0.10	4.10±0.41	0.95±0.09	0.00±0.00	0.73±0.07	0.45±0.03	0.10±0.01	1.27±0.07
AS87-3	180–250	20±5	0.81±0.08	3.22±0.32	1.13±0.11	0.00±0.00	0.79±0.08	0.43±0.03	0.09±0.01	1.31±0.09
V / AS75: 25°42'53"N, 32°36'41"E; 75.7 m.a.s.l.										
AS75-1	150–210	20±5	0.97±0.10	2.97±0.30	1.09±0.11	0.00±0.00	0.81±0.08	0.43±0.03	0.12±0.01	1.35±0.09
AS75-2	180–210	20±5	1.02±0.10	3.30±0.33	1.05±0.10	0.00±0.00	0.77±0.07	0.43±0.03	0.10±0.01	1.30±0.08
AS75-3	180–210	25±5	0.53±0.05	1.79±0.18	0.97±0.10	0.00±0.00	0.62±0.06	0.30±0.03	0.08±0.01	1.00±0.07
AS75-4	180–210	25±5	0.52±0.05	1.86±0.19	1.05±0.11	0.00±0.00	0.67±0.07	0.32±0.03	0.08±0.01	1.06±0.08
VI / AS76: 25°42'49"N, 32°36'47"E; 75.8 m.a.s.l.										
AS76-1	150–180	25±5	0.97±0.10	3.23±0.32	1.06±0.11	0.00±0.00	0.75±0.07	0.41±0.03	0.10±0.01	1.25±0.08
AS76-2	150–180	25±5	1.10±0.11	3.54±0.35	1.03±0.10	0.00±0.00	0.75±0.07	0.43±0.03	0.10±0.01	1.27±0.08
VII / AS107: 25°42'49"N, 32°36'50"E; 75.8 m.a.s.l.										
AS107-1	4–11	10±5	1.34±0.13	5.22±0.52	0.92±0.11	0.22±0.03	0.95±0.10	0.56±0.05	0.21±0.02	1.94±0.11
AS107-2	4–11	15±5	1.31±0.13	5.26±0.53	0.97±0.11	0.20±0.02	0.93±0.09	0.55±0.04	0.17±0.02	1.85±0.11
AS107-3	4–11	20±5	1.10±0.11	4.60±0.46	1.04±0.11	0.16±0.02	0.89±0.09	0.49±0.04	0.15±0.02	1.69±0.10
AS107-4	4–11	20±5	1.10±0.11	4.61±0.46	1.00±0.11	0.16±0.02	0.86±0.08	0.48±0.04	0.13±0.01	1.64±0.10
AS107-5	4–11	20±5	0.99±0.10	4.46±0.45	1.00±0.11	0.15±0.02	0.85±0.08	0.47±0.04	0.12±0.01	1.58±0.09
AS107-6	4–11	20±5	1.10±0.11	4.35±0.44	1.00±0.11	0.16±0.02	0.86±0.08	0.47±0.04	0.11±0.01	1.59±0.09
AS107-7	4–11	25±5	1.00±0.10	4.15±0.42	1.03±0.11	0.14±0.02	0.82±0.08	0.44±0.03	0.10±0.01	1.50±0.09
AS107-8	4–11	25±5	1.19±0.12	3.94±0.39	0.93±0.11	0.15±0.02	0.78±0.08	0.43±0.03	0.09±0.01	1.44±0.09
AS107-9	150–250	25±5	0.83±0.08	2.56±0.26	1.06±0.11	0.00±0.00	0.71±0.07	0.37±0.03	0.08±0.01	1.16±0.08
VIII / AS77: 25°42'46"N, 32°36'54"E; 76.0 m.a.s.l.										
AS77-1	90–210	25±5	1.64±0.16	3.96±0.40	1.11±0.11	0.00±0.00	0.85±0.08	0.51±0.04	0.07±0.01	1.43±0.09
AS77-2	180–210	25±5	0.93±0.09	4.19±0.42	1.13±0.11	0.00±0.00	0.79±0.07	0.46±0.03	0.07±0.01	1.31±0.08
IX / AS145: 25°42'38"N, 32°37'12"E; 76.1 m.a.s.l.										
AS145-1	90–210	20±5	0.97±0.10	3.25±0.33	1.03±0.10	0.00±0.00	0.77±0.07	0.42±0.03	0.09±0.01	1.29±0.08
AS145-2	90–250	20±5	1.41±0.14	5.40±0.54	0.75±0.08	0.00±0.00	0.67±0.06	0.49±0.04	0.09±0.01	1.25±0.07
X / AS82: 25°42'34"N, 32°37'23"E; 76.2 m.a.s.l.										
AS82-1	180–250	20±5	0.82±0.08	2.66±0.27	1.12±0.11	0.00±0.00	0.78±0.08	0.41±0.03	0.11±0.01	1.29±0.08
AS82-2	150–250	20±5	1.13±0.11	3.23±0.32	1.05±0.10	0.00±0.00	0.78±0.07	0.44±0.03	0.10±0.01	1.32±0.08
AS82-3	180–210	25±5	0.49±0.05	1.56±0.16	0.85±0.08	0.00±0.00	0.55±0.05	0.27±0.02	0.07±0.01	0.89±0.06
AS82-4	180–210	25±5	0.62±0.06	2.50±0.25	1.15±0.11	0.00±0.00	0.74±0.07	0.37±0.03	0.07±0.01	1.18±0.08
XI / AS89: 25°42'19"N, 32°37'53"E; 76.3 m.a.s.l.										
AS89-1	180–210	5±2	0.92±0.09	2.78±0.28	1.02±0.10	0.00±0.00	0.87±0.07	0.46±0.03	0.17±0.02	1.50±0.08
XII / PC32: 25°43'02"N, 32°39'52"E; 76.7 m.a.s.l.										
PC32-1	150–210	25±5	1.05±0.10	3.58±0.36	1.10±0.11	0.00±0.00	0.78±0.07	0.44±0.03	0.08±0.01	1.29±0.08
PC32-2	180–210	25±5	0.97±0.10	3.19±0.32	1.07±0.11	0.00±0.00	0.74±0.07	0.41±0.03	0.08±0.01	1.23±0.08
XIII / AS118: 25°42'43"N, 32°40'22"E; 75.2 m.a.s.l.										
AS118-1	180–210	10±5	0.85±0.09	5.22±0.52	0.73±0.07	0.00±0.00	0.66±0.06	0.47±0.04	0.13±0.01	1.27±0.07
AS118-2	180–210	15±5	0.54±0.05	2.26±0.23	0.89±0.09	0.00±0.00	0.65±0.07	0.33±0.03	0.11±0.01	1.09±0.07
XIV / AS119: 25°42'40"N, 32°40'26"E; 75.2 m.a.s.l.										
AS119-1	180–210	15±5	0.78±0.08	2.76±0.28	0.90±0.11	0.00±0.00	0.69±0.08	0.38±0.03	0.11±0.01	1.18±0.09
AS119-2	180–210	15±5	0.35±0.03	1.07±0.11	0.64±0.11	0.00±0.00	0.45±0.07	0.21±0.03	0.11±0.01	0.78±0.08
XV / PC38: 25°42'38"N, 32°40'30"E; 75.2 m.a.s.l.										
PC38-1	4–11	25±5	0.79±0.08	2.92±0.29	1.09±0.11	0.10±0.01	0.81±0.08	0.39±0.03	0.09±0.01	1.39±0.09
PC38-2	4–11	25±5	0.73±0.07	3.09±0.31	1.04±0.11	0.10±0.01	0.78±0.08	0.38±0.03	0.09±0.01	1.34±0.08
XVI / AS131: 25°42'06"N, 32°41'04"E; 75.3 m.a.s.l.										
AS131-1	180–210	15±5	1.00±0.10	4.67±0.47	0.56±0.06	0.00±0.00	0.53±0.05	0.41±0.03	0.11±0.01	1.04±0.06
AS131-2	180–210	15±5	0.39±0.04	1.22±0.12	0.63±0.06	0.00±0.00	0.45±0.05	0.22±0.02	0.11±0.01	0.78±0.05
XVII / AS136: 25°41'31"N, 32°41'46"E; 75.8 m.a.s.l.										
AS136-1	180–210	10±5	0.57±0.06	2.78±0.28	0.64±0.06	0.00±0.00	0.53±0.05	0.32±0.03	0.17±0.02	1.02±0.06
AS136-2	180–210	10±5	0.56±0.06	1.72±0.17	0.68±0.07	0.00±0.00	0.54±0.06	0.28±0.02	0.15±0.02	0.97±0.06
XVIII / AS141: 25°41'13"N, 32°42'10"E; 79.0 m.a.s.l.										
AS141-1	180–210	5±2	0.66±0.07	2.17±0.22	0.83±0.08	0.00±0.00	0.69±0.06	0.36±0.02	0.17±0.02	1.22±0.07
AS141-2	180–210	10±5	0.71±0.07	2.90±0.29	1.00±0.10	0.00±0.00	0.79±0.08	0.42±0.03	0.13±0.01	1.33±0.09
AS141-3	180–210	10±5	0.99±0.10	4.91±0.49	1.00±0.10	0.00±0.00	0.85±0.08	0.53±0.04	0.12±0.01	1.50±0.09

Note: Coordinates are in degrees, minutes, and seconds (latitude/longitude); surface elevation is in meters above sea level (m.a.s.l.).

Extended Data Table 4 | Pre-heat plateau and dose recovery test summary

Sample	Combined pre-heat and dose recovery				Multi-grain dose recovery			Single grain dose recovery		
	Dose (Gy)	Accepted (measured)*	Temp (°C)	DR Ratio [†]	Dose (Gy)	Accepted (measured)*	DR Ratio [†]	Dose (Gy)	Accepted (measured)*	DR Ratio [†]
AS71-2	5	6 (6)	200	1.00±0.04	5	10 (12)	0.91±0.07	5	35 (700)	1.11±0.35
		5 (6)	220	0.90±0.04						
		6 (6)	240	0.97±0.10						
		5 (6)	260	1.00±0.07						
		5 (6)	200	1.02±0.11						
AS73-1	5	5 (6)	220	1.00±0.06	5	11 (12)	0.99±0.04	5	32 (700)	1.12±0.25
		6 (6)	240	0.96±0.09						
		6 (6)	260	0.97±0.12						
AS82-3	5	-	-	-	5	9 (12)	0.95±0.06	5	36 (700)	1.22±0.30
AS87-2	5	-	-	-	5	10 (12)	0.95±0.08	5	25 (700)	1.05±0.29
AS107-7	5	-	-	-	5	12 (12)	0.97±0.04	-	-	-
AS113-1	5	-	-	-	5	12 (12)	0.95±0.05	5	31 (700)	0.99±0.31
AS118-1	15	5 (6)	200	1.02±0.04	5	12 (12)	0.96±0.07	5	15 (700)	1.12±0.43
		6 (6)	220	0.99±0.08						
		6 (6)	240	1.03±0.09						
		6 (6)	260	1.06±0.08						
AS141-2	15	-	-	-	15	12 (12)	0.92±0.05	15	22 (700)	0.98±0.29
Average [§]		16 (18)	220	0.96±0.07		88 (96)	0.95±0.06		196 (4900)	1.07±0.28

*The number of signals passing all rejection criteria (accepted) are shown, alongside the number of measured signals.
[†]DR ratio is the ratio between the measured and administered dose. The average and standard deviation are shown.
[§]The average data for all measured samples.

Extended Data Table 5 | Egyptian cultural periods

Time period	Abbreviation	Dynasty (inclusive)	Age (BCE)	Age (ka)	Reference
Modern Egypt	ME	n/a	AD1798–now	0.2–now	Wensink et al., 2012 ⁽⁶⁸⁾
Islamic Egypt	IE	n/a	AD642–1798	1.4–0.2	Wensink et al., 2012 ⁽⁶⁸⁾
Roman and Byzantine Period	RBP	n/a	30BCE–AD642	2.1–1.4	Lloyd, 2010 ⁽⁶⁹⁾ ; Wensink et al., 2012 ⁽⁶⁸⁾
Macedonian and Ptolemaic Periods	PP	n/a	332–30	2.4–2.1	Hornung et al., 2006 ⁽⁷⁰⁾
Late Period	LP	D26–D31	664–332	2.7–2.4	Hornung et al., 2006 ⁽⁷⁰⁾ ; Payraudeau, 2020 ⁽⁷¹⁾
Third Intermediate Period	TIP	D21–D25	1076–664	3.1–2.7	Hornung et al., 2006 ⁽⁷⁰⁾
New Kingdom	NK	D18–D20	1539–1077	3.6–3.1	Hornung et al., 2006 ⁽⁷⁰⁾
Second Intermediate Period	SIP / II	D16–D17	1759–1539	3.8–3.6	Hornung et al., 2006 ⁽⁷⁰⁾
Middle Kingdom	M(K)	Late D11–D13	1980–1760	4.0–3.8	Hornung et al., 2006 ⁽⁷⁰⁾
First Intermediate Period	FIP / I	D8–Early D11	2152–1980	4.1–4.0	Hornung et al., 2006 ⁽⁷⁰⁾
Old Kingdom	OK	D3–D6	2592–2152	4.6–4.1	Hornung et al., 2006 ⁽⁷⁰⁾
Early Dynastic	ED	D1–D2	3100–2592	5.1–4.6	Hornung et al., 2006 ⁽⁷⁰⁾ ; Dee et al., 2013 ⁽⁷²⁾
Predynastic (Naqada) Period	Pre	n/a	3900–3100	5.9–5.1	Dee et al., 2013 ⁽⁷²⁾ ; Tassie, 2014 ⁽⁷³⁾
Neolithic Period	Neol	n/a	5500–3900	7.5–5.9	Tassie, 2014 ⁽⁷³⁾
Epipaleolithic Period	Epipal	n/a	11000–5500	13.0–7.5	Tassie, 2014 ⁽⁷³⁾
Late Palaeolithic	LatePal	n/a	25000–11000	27.0–13.0	Tassie, 2014 ⁽⁷³⁾

References: Wensink et al., 2012⁶⁸; Lloyd, 2010⁶⁹; Hornung et al., 2006⁷⁰; Payraudeau, 2020⁷¹; Dee et al., 2013⁷² and Tassie, 2014⁷³.